A WEARABLE ANTENNA SYSTEM FOR STRUCTURAL MONITORING OF BIODEGRADABLE MAGNESIUM-BASED SUTURE WIRES

by

Ozan Furkan Sezgen

B.S., Electrical and Electronics Engineering, Istanbul Bilgi University, 2018

Submitted to the Institute for Graduate Studies in
Science and Engineering in partial fulfillment of
the requirements for the degree of
Master of Science

Graduate Program in Electrical and Electronics Engineering

Boğaziçi University

2022

ACKNOWLEDGEMENTS

I would like to express my gratitude to my supervisor Sema Dumanlı Oktar, first and foremost, for her mentorship, endless support, patience, and guidance throughout the years that I had the privilege to work with her. This work could not have become what it is without her invaluable contribution.

I would also show my appreciation to Prof. Arda Deniz Yalçınkaya and Assist. Prof. Zeliha Cansu Canbek Özdil for joining to my thesis committee.

I would also like to give special thanks to all members of BOUNTENNA Research Laboratory for their contributions to this work and their friendship. I will never forget fun times I spent here with them.

I would also show my appreciation to Uzay Bengi, Oğuz Kaan Erden, Merve Görkem Durmaz and Zeynep Yetişken for unlimited support and help through my thesis process.

I would like to give huge thanks to Ahmet Bilir, who helped me in the last phase of my thesis and took measurements with me for hours.

Last but most definitely not the least, I would like to express my profound gratitude to my beloved parents Beyit and Ayfer, and my dear sister, Ezgi, for their endless support, encouragements, and unconditional love throughout my journey. None of my achievements would have been possible without them and I would like to dedicate this thesis to them.

ABSTRACT

A WEARABLE ANTENNA SYSTEM FOR STRUCTURAL MONITORING OF BIODEGRADABLE MAGNESIUM-BASED SUTURE WIRES

Open-heart surgery is a way of treating various heart problems. It is a challenging operation during which the operating surgeon will cut through the sternum and spread the ribcage to access the heart. After sternotomy, complications such as sternal separation and wound or subcutaneous infections may occur due to the sensitivity of the operation region. The probability of occurrence for these post-operative infections is low; however, the mortality rate is high in case of infection. Such risks make remote monitoring and examining patients' health more critical in the post-operative period. Computed tomography appears as the traditional way of tracking the sutures surrounding the sternum. Stainless steel and titanium are popular for sutures to close the sternum after open-heart surgery. This thesis proposes an alternative suture material and a novel structural real-time monitoring technique in the post-operative period. Magnesium-based sutures have become significant in medical applications due to their biocompatibility and its ability to degrade without releasing any byproduct. A wearable antenna system is a possible solution to monitor patients who underwent open-heart surgery. Ultra-wideband(UWB) coplanar waveguide(CPW) fed disc monopole antenna is chosen as the on-body reader antenna and is optimized to operate on the human body and is fabricated on 1.27 mm Rogers RO3210 with relative permittivity of 10.2. Next, a series of analyses are made in the numerical model, such as the degradation tracking of magnesium-based sutures, breakage points on the suture, different thicknesses to represent overweight and underweight patients, and antenna position effect. After that, the measurement setup is established, including the tissue-mimicking human average and human bone phantoms. Finally, simulation and measurement results are compared and interpreted.

ÖZET

BİYOBOZUNUR MAGNEZYUM ESASLI DİKİŞ TELLERİNİN YAPISAL İZLENMESİ İÇİN GİYİLEBİLİR BİR ANTEN SİSTEMİ

Açık kalp ameliyatı, çeşitli kalp problemlerini tedavi etmenin bir yoludur. Ameliyat eden cerrahın sternumu keseceği ve kalbe erişmek için göğüs kafesini açacağı zorlu bir ameliyattır. Sternotomi sonrası operasyon bölgesinin hassasiyetine bağlı olarak sternal ayrılma ve yara veya deri altı enfeksiyon gibi komplikasyonlar ortaya çıkabilir. Bu ameliyat sonrası enfeksiyonların ortaya çıkma olasılığı düşüktür; ancak enfeksiyon durumunda ölüm oranı yüksektir. Bu tür riskler, ameliyat sonrası dönemde hastaların sağlığının uzaktan izlenmesini ve incelenmesini daha kritik hale getirmektedir. Bilgisayarlı tomografi, sternumu çevreleyen dikişleri izlemenin geleneksel yolu olarak ortaya çıkıyor. Açık kalp ameliyatından sonra sternumu kapatmak için dikişlerde paslanmaz çelik ve titanyum popüler seçeneklerdir. Bu tez, ameliyat sonrası dönemde alternatif bir sütür materyali ve yeni bir yapısal gerçek zamanlı izleme tekniği önermektedir. Magnezyum bazlı sütürler, magnezyumun biyouyumluluğu ve herhangi bir yan ürün bırakmadan bozunma kabiliyeti nedeniyle tıbbi uygulamalarda önemli hale gelmiştir. Giyilebilir bir anten sistemi, açık kalp ameliyatı geçiren hastaları izlemek için olası bir çözümdür. Vücut üstü okuyucu anten olarak ultra geniş bant (UWB) eş düzlemli dalga kılavuzu (CPW) beslemeli disk monopol anten seçilmiştir ve insan vücudunda çalışmak üzere optimize edilmiştir ve göreceli geçirgenliği 10.2 olan 1.27 mm Rogers RO3210 üzerinde üretilmiştir. Daha sonra, magnezyum bazlı sütürlerin bozulma takibi, sütür üzerindeki kırılma noktaları, fazla kilolu ve düşük kilolu hastaları temsil etmek için farklı kalınlıklar ve anten pozisyonu etkisi gibi sayısal modelde bir dizi analiz yapılır. Bundan sonra, dokuyu taklit eden insan ortalamasını ve insan kemiği fantomlarını içeren ölçüm düzeni kurulur. Son olarak simülasyon ve ölçüm sonuçları karşılaştırılır ve yorumlanır.

TABLE OF CONTENTS

LIST OF FIGURES

LIST OF TABLES

LIST OF SYMBOLS

λ	wavelength of free space
θ	Elevation Degree
Ω	Unit of Electrical Resistance
ε_0	relative permittivity of free space
ε_1	relative permittivity of dielectric substrate
ε_2	relative permittivity of dielectric substrate
ε_{eff}	effective permittivity
σ	conductivity of the medium
$\tan(\delta)$	loss tangent
l	Lenght of Dipole Antenna
$Z_{monopole}$	Characteristics Impedance of Monopole Antenna
Z_{dipole}	Characteristic Impedance of Dipole Antenna
Z_0	Characteristic Impedance
C_{CPW}	total capacitance of the CPW
C_1	partial capacitance of the lower dielectric substrate
C_2	partial capacitance of the upper dielectric substrate
C_{air}	Capacitance of the CPW in the absence of all dielectric layers
v_{ph}	phase velocity
q_1	partial filling factor
q_2	partial filling factor
S	Siemens

LIST OF ACRONYMS/ABBREVIATIONS

2D	Two Dimensional
3D	Three Dimensional
CT	Computed Tomography
CPW	Coplanar Waveguide
DAK	Dielectric Assessment Kit
dB	Decibel
DSWI	Deep Surgical Wound Infections
Fe	Iron
FR4	Flame Retardant 4
GHz	Gigahertz
GPa	GigaPascal
HFSS	High Frequency Simulation Software
LPKF	Leiterplatten-Kopierfr¨asen
Mg	Magnesium
$MgCl_2$	Magnesium Chloride
$Mg(OH)_2$	Magnesium Hydroxide
MPa	Megapascal
OH	Hydroxide
pH	Potential of Hydrogen
PLA	Polylactic acid
RDI	Recommended Daily Intake
SLA	Stereolithography
UWB	Ultra Wide-Band
VNA	Vector Network Analyzer
WBAN	Wireless Body Area Network
WHO	World Health Organization
Zn	Zinc

1. INTRODUCTION

1.1. General View of Heart Diseases

Heart diseases limit the heart's vital functions and are the leading cause of death for people in the United States [1]. More than 600,000 people in the United States die from heart diseases each year [2]. The cost of heart-related complications was about $363 billion annually from 2016 to 2017, including medical expenses, medicines, and low productivity because of deaths [2].

In 2020-2021, about 950 thousand inpatients experienced circulatory system diseases such as coronary heart disease and cardiovascular disease in the United Kingdom, and coronary heart disease and cardiovascular disease caused 99 and 255 deaths per 100,0000 population, respectively [3]. Also, 14,030 coronary artery bypass surgeries were operated on in 2020 [3–7]. According to a British Heart Foundation report, in 2022, healthcare costs for heart and circulatory diseases are estimated to be £9 billion [7].

Open-heart surgery is a way of treating heart problems, and during the procedure, it is necessary to cut through the sternum and spread the ribcage to access the heart [8]. Since it is a challenging operation, there is always a risk of complications such as losing the integrity of the sternum, blood coming out of the sternotomy, inflammation, or subcutaneous infection in the chest area due to the sensitivity of the operating environment.

1.2. Postoperative Process of Open-Heart Surgery

There is always a risk of having infections during the post-operative process. Surgical site infection is an infection that occurs after surgery where the surgery took place [9]. The infection can be a superficial or deep wound infection. Deep sternal infections are potentially life-threatening complications [9]. Several studies show that

the probability of occurrence of these post-operative infections is low. However, the mortality rate is high. In [10], out of 9,201 patients who experienced a coronary artery bypass grafting in Tehran Heart Center from 2002 to 2006, 44 of them had sternal wound infections (0.47%), and 21 of them had deep surgical wound infections (DSWI) (0.22%). The mortality rate of those infected is 9.1% and 14%, respectively. Also, as stated in [11], 2,835 out of 176,537 patients who had at least one cardiac surgery from 2009 to 2013 in the United States underwent DSWI, and the mortality rate reached 10.7%. In addition, the same study shows the hospital stays of patients with DSWI can reach up to 30 days, and the average cost can be 2.5 times higher compared to those without DSWI.

In the post-operative period, patient monitoring becomes vital for detecting whether such complications occur. An X-ray is an imaging tool of the chest area in the post-operative period. There are risks associated with using X-ray imaging, which uses ionizing radiation to generate images of the body. Ionizing radiation is a form of radiation with enough energy to cause damage to human DNA potentially. Therefore, they are still classed as a carcinogen by the World Health Organization (WHO). Also, x-rays can cause an economic burden on the country's economy. The national average cost for a privately funded chest X-ray is around £100, according to Private Healthcare UK, and in May 2020, about 950,000 X-rays were performed in the UK.

Computed tomography (CT) is one of the types of X-rays which gives the largest dose of X-rays to track post-operative progress around the sternum [12]. The patient lies on a table and enters a ring-shaped scanner. This procedure uses the highest dose of X-rays because many images are taken in one sitting. Each scan brings about 1 to 10 mSv to the human body, depending on the dose of radiation and the part of the body being exposed [13]. While a low-dose chest CT scan yields around 1.5 mSv, the radiation dose can rise to 8 mSv at the full-dose application [13]. The average value of a CT chest scan is 6.1 mSv, equal to the total natural background radiation dose accumulated in 2 years.

Radiation also damages cells that grow and divide rapidly, such as breasts, lungs, and thyroid glands. Therefore, some organs are more vulnerable to radiation [14]. Also, CT scans in children may triple the risk of brain cancer and leukemia, especially when administered to the abdomen and chest at certain doses.

CT, moreover, increases healthcare costs drastically. In France, the CT scanning volume can be estimated to be €7.2 million in 2016 [15]. From a National Health Insurance perspective, the CT-scan total unit cost can be estimated to be €102.66 [15].

Considering these drawbacks of current tracking systems, an alternative solution is clearly required. Here, we are proposing a monitoring system that is superior to the existing systems in two ways. First of all, the proposed system is a real-time continuous monitoring system that is portable; hence the monitoring can be extended to the patient's daily life. Secondly, the tracking is performed using non-ionizing electromagnetic waves in the region of microwave frequency range where most of the wireless communication systems operate. The radiated power from such devices has been proven harmless to the human body with the maximum power transmission limitations in place. Note that this monitoring is only possible if a biodegradable suture similar to the one utilized here in this thesis is used. We aim to link the degradation speed with infection and track the degradation [16, 17]. The degradation speed of Mg *in-vivo* increases in case of deep wound infection.

Here the degradation is going to be tracked. This also opens doors to another level of monitoring: the structural monitoring of the suture. Even if there is no infection, the monitoring system will track any breakages that might occur during the healing process. The choice of the suture material utilized here and its justification will be discussed further in Section 1.4.

1.3. Suture Materials Currently Used in Medicine

Surgical suture is a method to promote closure and healing of surgical wounds by upholding tissues together, which started with the use of fibres in flax hundreds of

years ago [18]. Today, various polymers and metals are preferred as the suture material [19, 20]. Studies prove that sutures have become an efficient and crucial element of surgeries.

Suture materials must fulfill specific requirements. In general, the ideal suture should have significant flexibility for better handling characteristics, maintain integrity during planned usage time, exhibit biocompatibility, ease in knot placement, and have high knot security [21–28]. Suture materials can be classified into two categories according to their structures: degradable and non-degradable. Degradable materials can be defined as a material dissolved in the human body in time, avoiding the need for a second surgical intervention to remove them after healing. However, non-degradable materials remain in the surgical site until a removal operation is applied.

Since the 1950s, synthetic polymers and stainless steel have been the most used materials for suture applications [19, 20]. Polymer sutures are especially preferred to stitch soft tissues since they cannot withstand high loads efficiently. Also, low creep and stress relaxation resistance cause them to have a narrow range of implementations [29]. Therefore, polymers cannot be considered a good candidate for sternal closure after surgical intervention. Stainless steel possesses higher strength and better creep and relaxation behavior than polymers [30, 31]. Thus, it provides more practical use in hard tissue applications.

1.4. Magnesium As a Suture Material, Comparison With Other Alternatives and The Proposed Magnesium Suture

Studies based on degradable metals have become an intensely heated debate topic in the last few years. Magnesium(Mg), Iron(Fe), Zinc(Zn) and their alloys have been demonstrated as bioabsorbable implant metals [32–35]. Mg and its alloys have been extensively investigated in recent decades due to several properties that make them a suitable choice for biodegradable material for medical applications. However, for magnesium and its alloys to be evaluated as biodegradable suture material, they should fulfill some requirements in terms of biocompatibility, mechanical properties,

and biodegradation process. Thus, magnesium sutures can open a door to a continuous monitoring mechanism for infection detection in the chest area in the postoperative period. Therefore, main properties of magnesium will be discussed in later sections.

1.4.1. Biocompatibility

Magnesium is well-tolerated by the body, with exceeding low toxicity and excretion, and displays numerous bioactive effects such as improved bone formation and protection against oxidate stresses. Magnesium plays a significant role in the human body since it enhances numerous physiological mechanisms in the human body and more than 300 enzymatic reactions, especially phosphate-dependent reactions [36–40]. In addition, the biocompatibility level of magnesium may vary because of the alloying metal's characteristics and density in the alloy. In [41–43], there is no in vitro adverse effects on vascular smooth muscle cells, human osteosarcoma cells, and human umbilical perivascular cell using a small extent of alloying metal.

It can also be interpreted by examining the recommended daily intake(RDI) for the human body to evaluate magnesium and other metals in terms of biocompatibility. While the given RDI for iron and zinc is relatively low, which is not more than 20 mg, [44–46] magnesium has 25 times higher RDI value, as shown in Figure 1.1 regenerated from [47] [48]. From this point of view, magnesium has become a more harmless option and stands out as the ideal metal. However, to make an accurate assessment, the material and its alloy degradation rates, degradation product properties, and body fluids effects must be studied in detail.

The highest and lowest corrosion rates and lower limit of RDI in the literature for three metals and their calculated mass loss range are demonstrated in [48]. Mg and Zn remain below the threshold during the corrosion process. Thus, magnesium appears particularly attractive due to its slow release for suture applications.

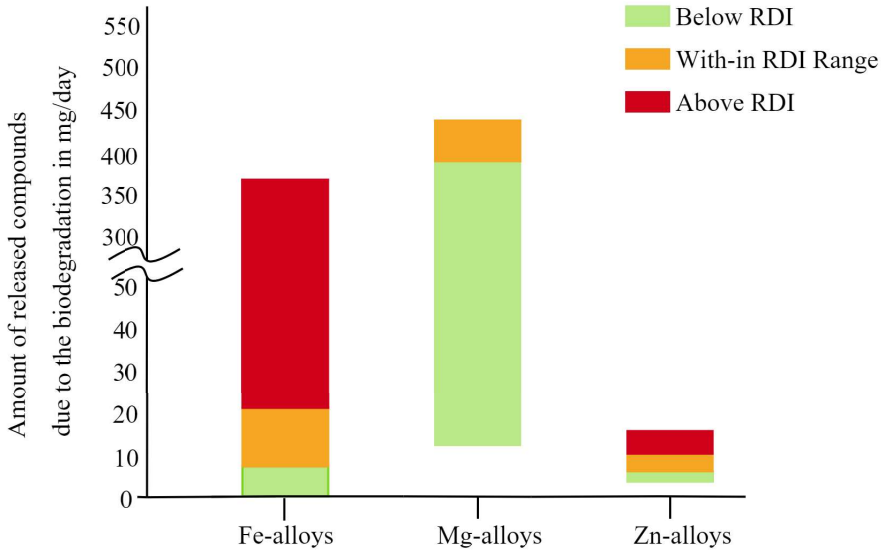

Figure 1.1. The concentration of released compounds during the biodegradation with RDI range [47].

1.4.2. Mechanical Properties

Moreover, all Mg alloys should meet a broad range of mechanical properties to be used for in-body applications. All main properties and their accepted range are shown in Table 1.1.

The main factor among the mechanical properties is the yield strength, which indicates the strength at which the deformation begins [48]. Materials with high yield strength are ideal for suture material because this indicates less chance of deformation at any point on the suture.

However, yield strength should always be considered with elastic properties to provide retention force without damaging the suture [48]. All three biodegradable metals have strength properties, which shows that they are suitable for soft tissue sutures, and Mg alloys have failed to meet the required strength properties to suture hard tissue. However, if greater wires or diameter are applied, Mg alloys can fulfill the minimum mechanical requirements [48].

Table 1.1. Mechanical properties and accepted range for Mg and its alloys to be used as a suture.

Mechanical Property	**Accepted Range**
Yield Strength	70 MPa to 220 MPa
Tensile Strength	193 MPa to 550 MPa
Elongation to Failure	2% to 30%
Young's Modulus	45 GPa

In [48], the elongation rate of magnesium remains significantly lower than polymers. Magnesium does not necessarily exhibit better mechanical strength than polymers for the value of ultimate strength at failure. However, the yield strength of magnesium is better than polymers. It should be the main measure for selecting magnesium for suture applications because plastic deformation at low stresses is not desirable.

The stress-strain curves of magnesium and several polymers provided by [20, 21] are compared. All polymers show a remarkably lower yield point than Mg, and conflicting polymers make it challenging to comment about yield properties precisely [48]. Also, in [49], the suitability of magnesium for knotting has been studied and demonstrated.

1.4.3. Biodegradation Process

Corrosion rates of Mg and its alloys are also intensely studied to figure out the biodegradation process of magnesium. The overall corrosion rate of Mg and its alloys in vitro is generally higher than the corrosion rate obtained in vivo. In vitro studies show that Mg alloys have higher corrosion rates (1-10 mm/year) compared to high purity magnesium (0.25-0.38 mm/year) [50–52].

In the degradation process shown in Figure 1.2, Mg degradation contains a sequence of redox reactions in vivo. When Mg interacts with body fluids, they cause magnesium to oxidize to Mg cation and produce electrons as follows

$$\mathrm{Mg} \longrightarrow \mathrm{Mg}^{2+} + 2\,\mathrm{e}^{-}. \tag{1.1}$$

The reaction between these electrons and water results in the formation of hydrogen gas and hydroxide [51, 52] expressed as

$$2\,\mathrm{H_2O} + 2\,\mathrm{e}^{-} \longrightarrow \mathrm{H_2} + 2\,\mathrm{OH}^{-}. \tag{1.2}$$

Also, the interaction of magnesium with hydroxide causes a protective coating of $\mathrm{Mg(OH)_2}$ on the magnesium given by

$$\mathrm{Mg}^{+2} + 2\,\mathrm{OH}^{-} \longrightarrow \mathrm{Mg(OH)_2}. \tag{1.3}$$

The protective coating of $\mathrm{Mg(OH)_2}$ causes the degradation process to slow. This layer, however, erodes over time as chloride ions react with magnesium, forming $\mathrm{MgCl_2}$ [53] as follows

$$\begin{aligned} \mathrm{Mg(OH)_2} + 2\,\mathrm{Cl}^{-} &\longrightarrow \mathrm{Mg(Cl)_2} + 2\,\mathrm{OH}^{-}. && (1.4)\\ &\longrightarrow \mathrm{Mg}^{+2} + 2\,\mathrm{Cl}^{-} + 2\,\mathrm{OH}^{-}. && (1.5) \end{aligned}$$

In the following periods, the accumulation of hydroxide in the vicinity of the Mg implant increases the pH level. It results in an excess concentration of calcium and phosphate ions [54]. As a result, a calcium phosphate precipitate forms on the metal oxide layer, attracting cells to the site [53]. Aggregated cells produce more degradation products on the substrate surface, enabling the degradation of greater parts of magnesium as shown in Figure 1.2.

The degradation of polymers and metals can result in a change in the pH value in the vicinity of the tissue [55–60]. It is essential to remain the pH value within human tissues constant at around 7 for the physiological functions of the human body to continue to work effectively [48]. As biodegradable metals and polymers degrade, they release ions that affect the pH surrounding tissue. While the degradation of metals alkalizes the surrounding the tissue by utilizing accumulated OH^- ions, most polymers shift the pH to the lower values by employing carboxyl acids [55–60]. While a decreased pH is caused by polymer degradation, which negatively affects tissue healing, Mg does not exhibit perifocal cellular damage in current clinical studies [61, 62]. Although iron has no definite effect on pH change, it is accepted that it changes pH because of releasing OH^-.

In [48], corrosion characteristics of magnesium to Zn, Fe, and polymers are compared. Zn and Fe-alloys have lower rates than soft tissue polymers (1.9 mm/year). Mg-alloys, however, degrade much faster than both polymers and other metals. This inadequate corrosion resistance limits the application of magnesium sutures due to the mismatch between the rapid material degradation and tissue or bone caused by the adverse effect of H_2 on surrounding bone tissue.

The corrosion rate measurements of the proposed Mg-based suture show that it has 1.5-2.5 mm/year corrosion rate. Also, the mechanical properties of the proposed mg-based suture are tabulated in Table 1.2.

Table 1.2. Mechanical properties of the proposed Mg-based suture.

Mechanical Property	**Measured Value**
Tensile Strength	150 MPa to 250 MPa
Ductility	10% to 20%
Modulus of Elasticity	40-50 GPa

1.5. Novelty of Our Study

- The first novel part of our study is degradation monitoring with a wearable antenna. In the literature, wearable antenna systems are utilized mainly for detecting breast cancer and monitoring heart activity. In [63], 20 monopole antennas array system, In [64], microwave textile sensor is made of a monopole antenna on cotton, In [65], an ultra-wideband microstrip patch antenna, in [66], a thin film based monopole antenna array, In [67], a wearable and flexible monopole antenna array and in [68], a wearable patch antenna, in [69], a UWB wearable microstrip circular patch antenna, in [70], UWB flexible and wearable textile antenna, in [71], wearable conformal antenna arrays and in [72], flexible 16 antenna array is employed for microwave breast imaging and diagnosis. In [73], it is studied to monitor chest expansion during sit-to-stand transitions to enhance sternal measures for patients experiencing sternotomy. In [74], blood pressure is tracked during the post-operative process by employing a wearable, non-invasive sensor. The impacts of steel sternotomy wires on UWB WBAN channel characteristics are analyzed in [75]. In [76–79], a measurement-based study on the impact of the aortic valve implant on the channel characteristics is investigated, especially the effect of sternotomy wires on the ultra-wideband (UWB) on-body channel characteristics. However, to the author's knowledge, there is no wearable antenna system for the structural monitoring of biodegradable implants.
- Also, we are aiming to make continuous infection monitoring of open-heart surgery in the post-operative period. This is only possible thanks to magnesium-based sutures. We can realize structural monitoring of magnesium which can be linked to infection since magnesium degrades faster in an acidic medium. Post-surgical infections result in an increase in the acidity level in the human body. Thus, the speed of degradation can be related to infections.

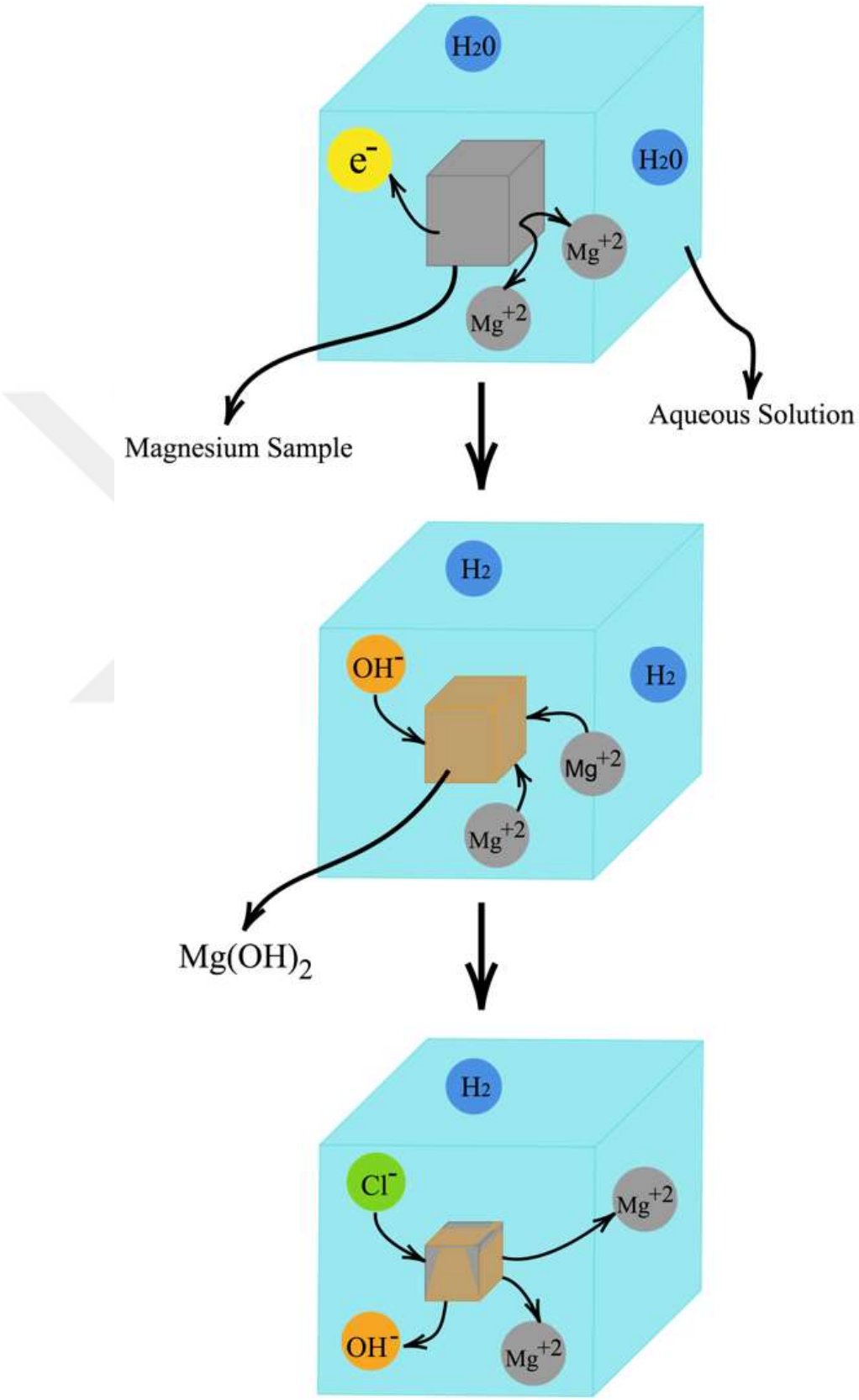

Figure 1.2. The degradation process of magnesium in aqueous solution.

2. ON-BODY READER ANTENNA SYSTEM

2.1. Image Theory

An obstacle, particularly one close to the radiating element, in a boundless medium can cause a significant change in the radiation characteristics of the antenna [80]. The ground is practically the most prevalent obstacle—any radiation from the radiating element directing the ground experiences a reflection. The ground's geometry and structural characteristics determine the amount of reflected energy and direction.

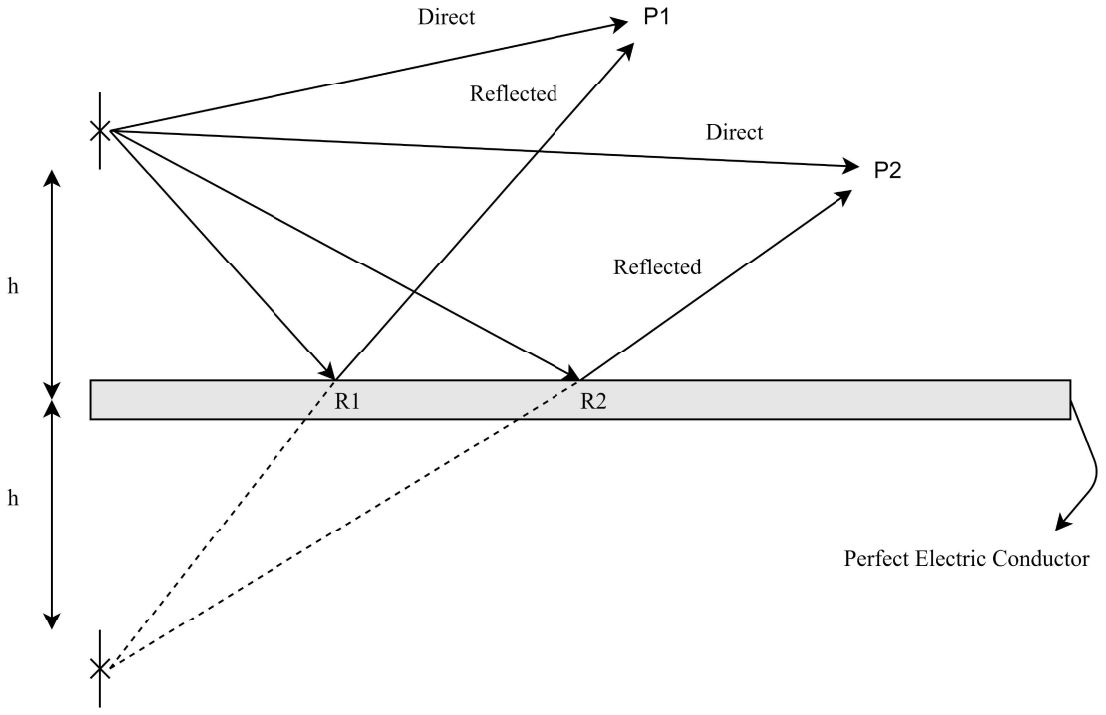

Figure 2.1. The representation of the image theory.

To study the performance of an antenna close to an infinite planar conductor, sources are created to account for reflections. These are imaginary ones. When paired with actual sources, they provide an equivalent system.

In Figure 2.1, a vertical dipole is assumed to be positioned a distance h above the ground. Energy from the source is radiated in all directions, determined by its bounded

directional properties. For an observation point P1, while there are direct waves to P1, a wave coming out of the main source experiences a reflection at the R1 point on the interface and reaches the P1 point in the shortest way in accordance with the reflection law. If the path it follows is extended below its ground, it is interpreted as coming from an imaginary point here. The distance of the virtual point to the ground is the same as the distance of the main point shown in Figure 2.1.

The amount of reflection is generally determined by the respective constitutive parameters of the medium on both sides of the boundary [80]. For below the interface, the incident wave is completely reflected and the field below the boundary does not exist. When boundary conditions are applied to the interface, the tangential components of the electric field must disappear at any point on the interface. Thus for an incident electric field with vertical polarization, the polarization of the reflected waves must be as indicated in Figure 2.2 to satisfy the boundary conditions. To excite the polarization of the reflected waves, the virtual source must also be vertical and with a polarity in the same direction as that of the actual source [80].

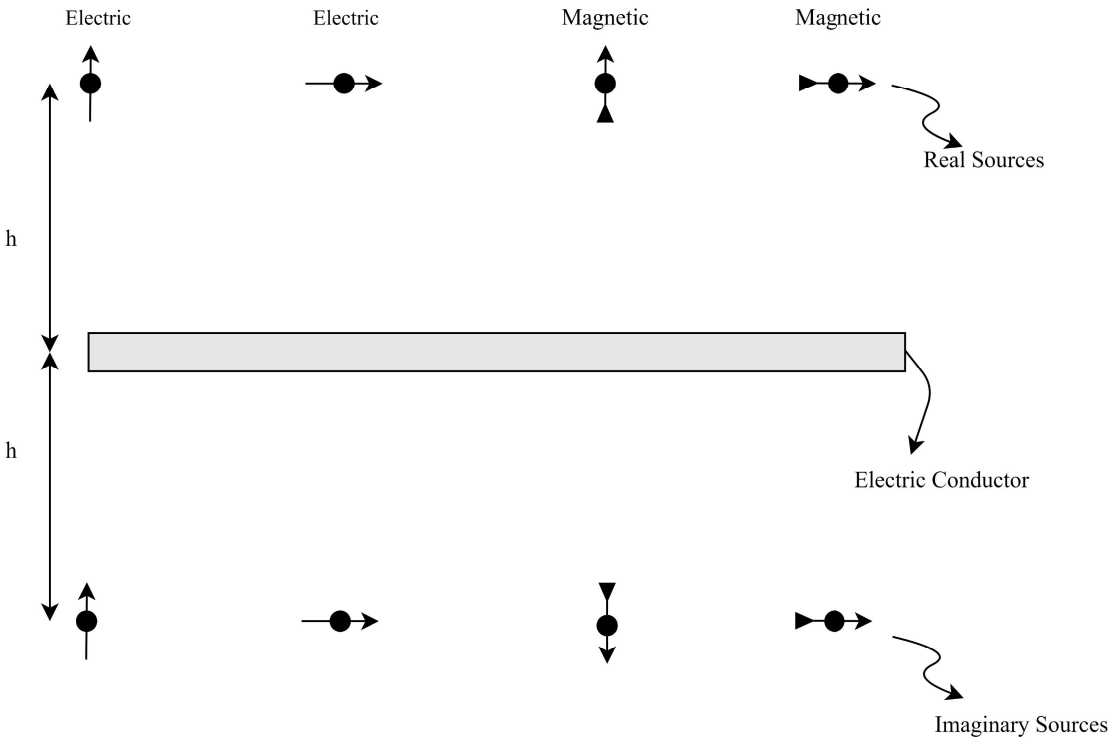

Figure 2.2. Image theory representation for different polarizations on the electric conductor surface.

2.2. Monopole Antenna and Dipole Antenna

The monopole antenna constitutes a group of derivatives of a dipole antenna. The half structure for a regular dipole antenna is called a monopole antenna [81]. The presence of the ground plane allows the monopole antenna to operate as electrically equivalent to a dipole antenna by replacing the lower half by image theory.

Due to the image theory, a monopole antenna's polarization of radiation and radiation patterns are the same as that of its equivalent dipole antenna. However, the monopole antenna has a field only at the top of half of the space, with zero radiation below the ground plane. In contrast, the equivalent dipole structure has fields on both sides, and the radiation to the bottom side is symmetric to that above. In this situation, the directivity of the monopole antenna is 3 dB bigger than the dipole antenna, which means it is twice in linear units.

In practice, a wide use has been made of a quarter-wavelength monopole ($l = \lambda/4$) mounted above a ground plane, as shown in Figure 2.3.

When applying image theory to this antenna, a $\lambda/4$ image is introduced, forming the $\lambda/2$ equivalent of Figure 2.3. It should be emphasized that $\lambda/2$ equivalent of Figure 2.3 gives the correct field values for the actual system of Figure 2.3 only above the ground. ($z \geq 0$, $0 \leq \theta \leq \pi/2$)

It follows that the input impedance of a $\lambda/4$ monopole antenna above a ground plane is equal to one-half that of an isolated $\lambda/2$ dipole. Thus, referred to as the maximum current, the input impedance of the monopole antenna is given by

$$Z_{monopole} = \frac{1}{2} \times Z_{dipole} \tag{2.1}$$

$$= \frac{1}{2}(73 + j42.5) = 36.5 + j21.25 \tag{2.2}$$

where $73 + j42.5$ is the input impedance of a $\lambda/2$ dipole at the maximum current.

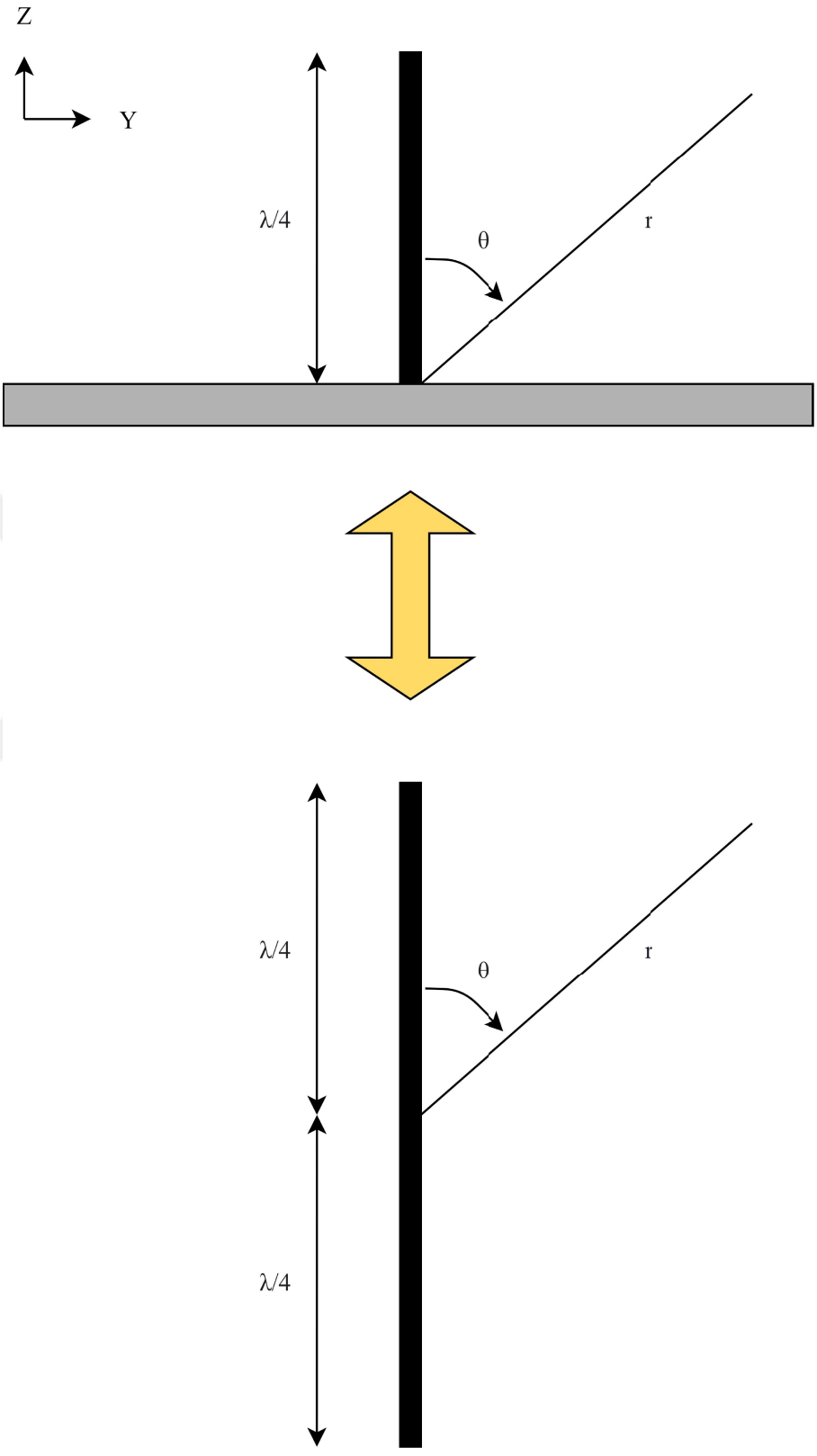

Figure 2.3. Monopole antenna as a dual of the dipole antenna.

2.3. Literature Review of Circular Disc Monopole Antenna

The circular disc monopole antenna has an increasing interest in communication systems. Since it has ultra-wide bandwidth characteristics, simple structure, and low-cost production [82]. However, numerous methods have been proposed to enhance the antenna matching over a broad bandwidth, including feeding optimizations, bevels, ground plane, and monopole shape modifications [83].

In [84], a circular disc monopole antenna is fed by 50 Ω microstrip feed line and is designed on FR4. In [83], [85, 86], the feeding mechanism is achieved using 50 Ω feed line and dual microstrip transition. Also, the feed line is tapered to improve input impedance matching in [87–89].

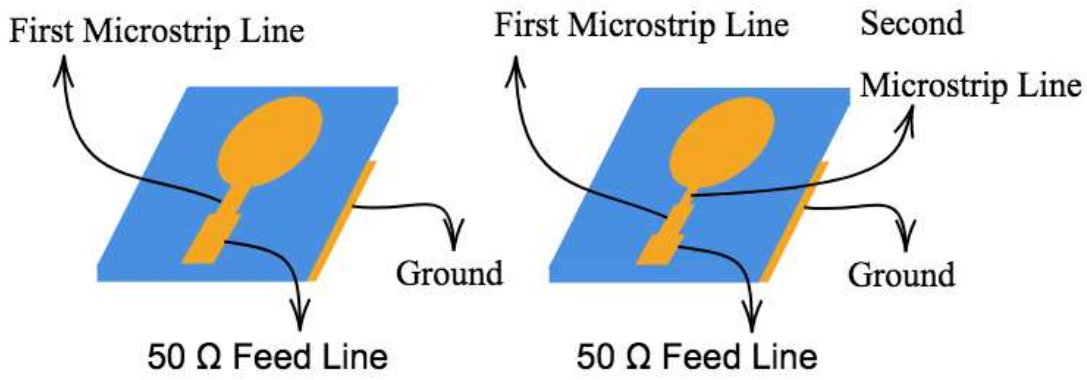

Figure 2.4. The different feed optimization techniques on circular disc monopole antenna.

Also, fractal geometry is frequently applied on disc, shown in Figure 2.5 re-generated from [90]. In [90–92], different shapes are tried. In addition, for the disc part, different shapes such as heart, monkey face, or rugby ball are replaced with the disc [93–95].

A switching mechanism also is added to the disc monopole antenna. The switch can cause monopole antenna to magnetic loop antenna [96]. In [97], disc monopole can convert UWB to narrowband through a switch. In [98], switching enables stepped rectangular monopole to convert into circular disc monopole.

Reconfiguration is an attractive topic for disc monopole antenna. It can be realized by using different stubs connecting to the ground or feed line [98]. Also, adding notch and slots to the ground can be utilized to achieve reconfiguration [99, 100].

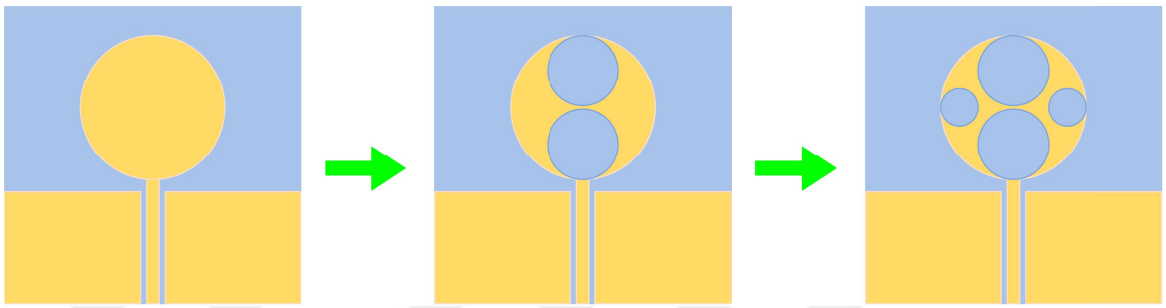

Figure 2.5. Fractal geometry application to circular disc monopole antenna [90].

Disc and ground shapes also experience different designs. In [88], edges around the circular monopole are tapered to improve impedance matching significantly, and rectangular gratings are added to tapered edges to enhance radiation characteristics. Semicircular disc and ground modification are also analyzed in [101, 102]. In [103], circular corner ground shape is studied. In [104], the disc is replaced with a rectangular patch and circular cuts are applied at the edges. In addition, ground optimization is analyzed in [105]. A novel design is proposed by adding two arc-shaped slots at the upper and lower side of the disc in [106]. UWB characteristic of the antenna is also maintained by adding U-shaped, L-shaped, and T-shaped slots in [107–110]. Also, adding between disc and feed is an alternative way to save UWB characteristic [111]. Also, a double circular disc is a solution to have UWB characteristics [112]. In [113], the disc is designed with a certain angle relative to the ground, and it is proposed to be used in wireless, satellite, and mobile communications. Moreover, circular disc monopole textile antenna and bending performance in analyzed in [114]. Dacron fabric is chosen as a substrate and woven copper thread as the conductor part of the antenna.

2.4. CPW-Monopole Antenna and Free Space Performance

An ultra-wide Band(UWB) coplanar waveguide(CPW) fed circular disc monopole antenna is chosen as an on-body reader antenna. Then, antenna designs, its optimization and simulations were carried out in ANSYS HFSS [115]. For the initial design, the antenna was proposed to be fabricated on a substrate with the dielectric constant of 3 [82]. The proposed CPW-fed circular disc monopole is shown in Figure 2.6 and its parameters are tabulated in Table 2.1.

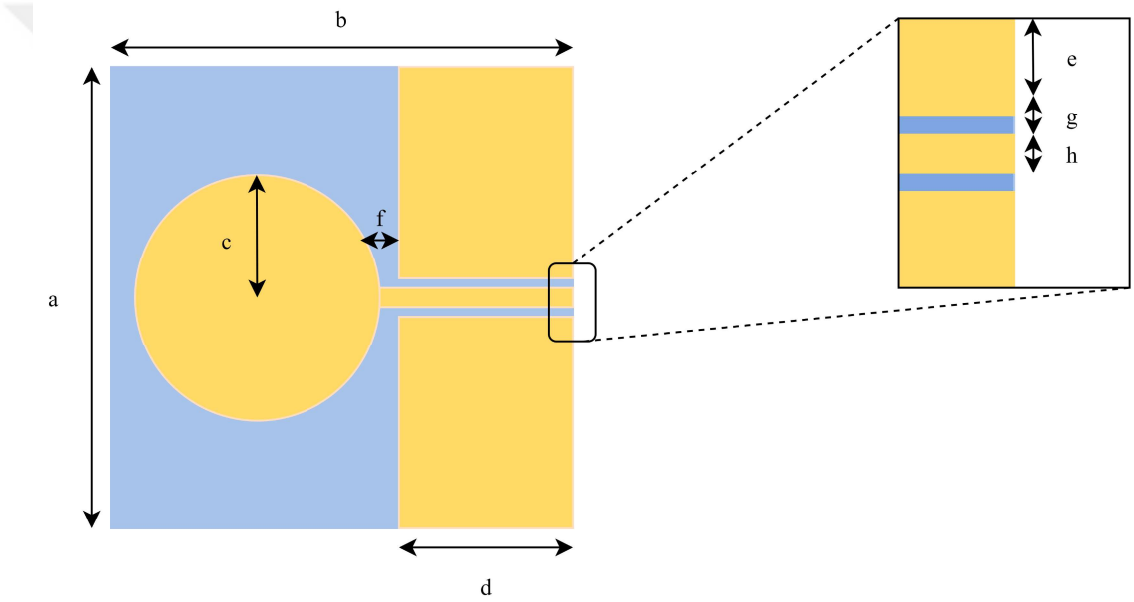

Figure 2.6. The proposed on-body reader antenna.

In Table 2.1, a and b describe the width and the length of the substrate,respectively. The disc radius is denoted as c. f is the gap between the disc and ground plane. d and e are described the width and the length of the ground. CPW parameters are also defined as g and h and they are taken 0.33 mm and 4 mm to achieve 50 Ω impedance, respectively. Also, a, b, c, d, e, and f are chosen 47 mm, 47 mm, 12.5 mm, 16.5 mm, 21.7 mm, 0.3 mm, respectively.

Figure 2.7 also shows that the first resonant frequency is determined by the diameter of the disc, which is approximately equal to the quarter of the guided wavelength at this frequency.

Table 2.1. The dimensions of the initial antenna design.

Antenna Dimension	Value (mm)
a	47
b	47
c	12.5
d	16.5
e	21.7
f	0.3
g	0.33
h	4

Also, the current distributions at three resonant frequencies are demonstrated in Figure 2.8. In the current distribution plots, the current is principally distributed along the circumference of the disc and the upper edge of the ground plane. It shows that these parameters can significantly control the antenna's bandwidth.

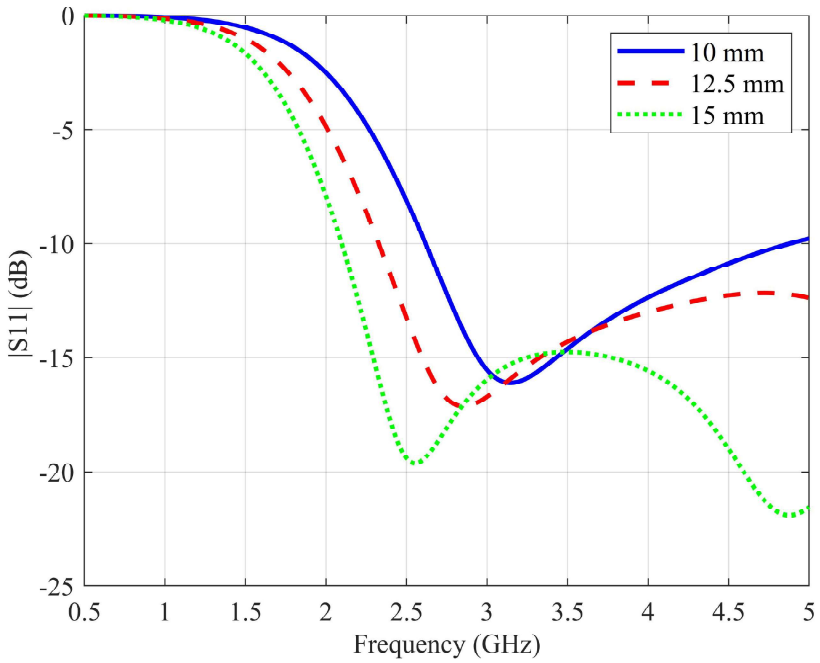

Figure 2.7. The effect of the disc radius on the lower end frequency of the UWB reader antenna.

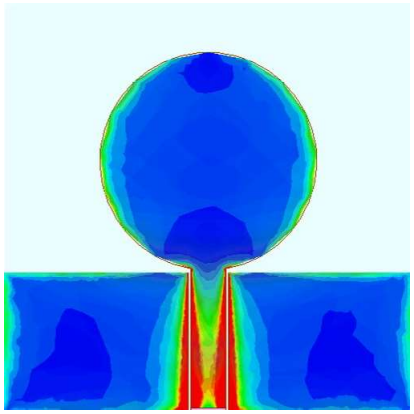

(a)

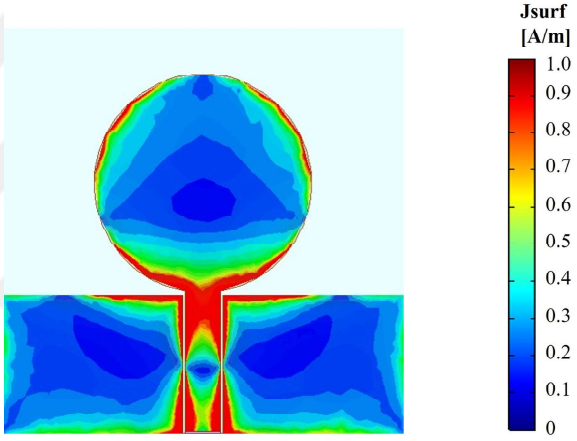

(b)

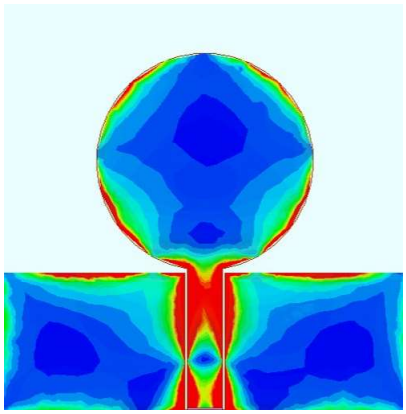

(c)

Figure 2.8. The current distribution of the reader antenna in free space at 2.8 GHz (a), 6.1 GHz (b), and 9 GHz (c).

Furthermore, It is proven that the first resonant frequency is directly associated with the radius of the circular disc, as can be seen in Figure 2.7. An increase in the diameter of the disc leads to a decrease in the resonant frequency. Thus, the lower end frequency of bandwidth of the antenna is directly determined by the diameter of the disc [82]. On the other hand, the higher resonance is controlled with f. The other parameters d and e control the input impedance.

The reflection coefficient of the antenna is shown in Figure 2.9. The antenna converges the -10 dB UWB bandwidth from 2.8 GHz to 10 GHz. In addition, the 3D radiation pattern of the antenna at the first resonant frequency of 2.8 GHz is shown in Figure 2.10.

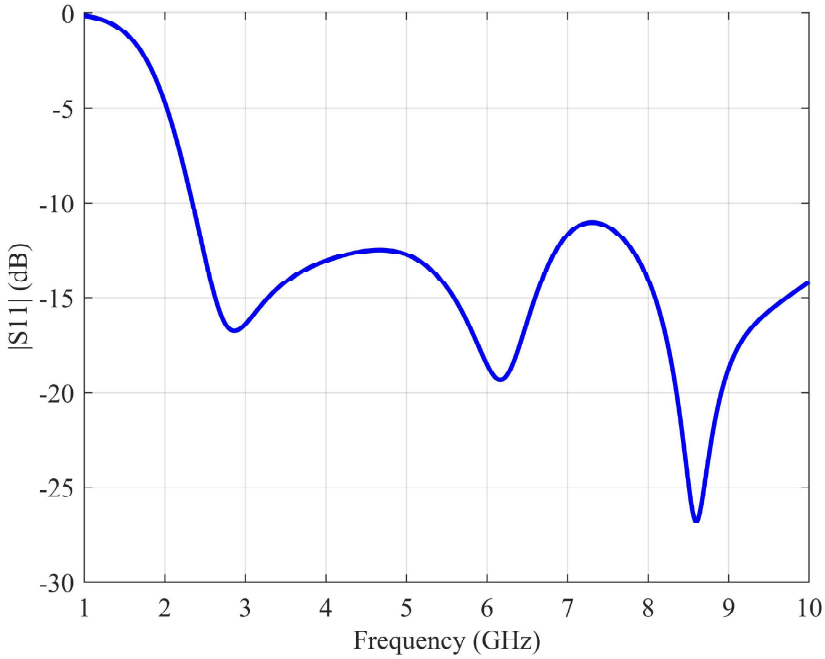

Figure 2.9. The reflection coefficient of the proposed on-body reader antenna.

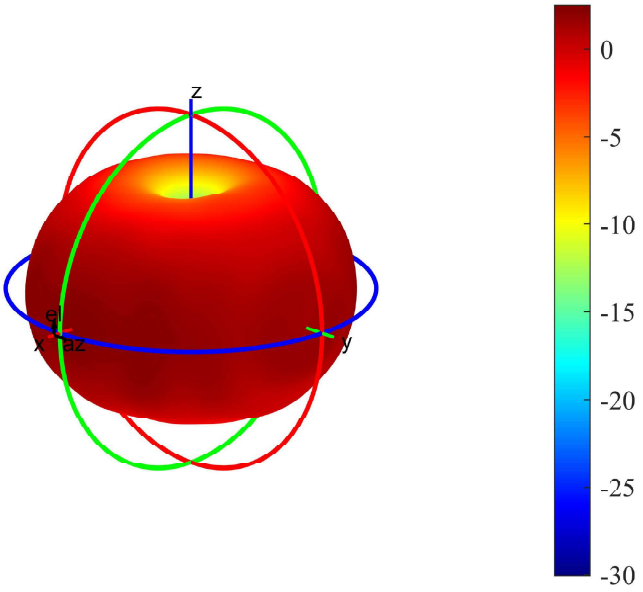

Figure 2.10. The 3D radiation pattern of the reader antenna at the first resonance of 2.8 GHz.

2.5. CPW-Monopole Antenna and On-Body Performance

2.5.1. Human Body Effect on Antenna

In Wireless Body Area Networks (WBAN) applications, antenna performance operating close to the human body undergoes critical changes due to the electrical characteristic of the human body which the antenna is exposed.

Human body tissues comprise various materials, including water, electrolytes, dissolved organic molecules, and ions. Molecules can interact with the electric field due to having a dipolar momentum. Furthermore, ion conduction and polarization effects are made possible by the presence of ions, which further play a significant role in the interaction with an electric field. This indicates that the human body absorbs energy from an electromagnetic field through its ionic activity.

Human body tissues are non-magnetic ($\mu_r'' = 0$). Therefore, electric permittivity is the most crucial factor influencing the electromagnetic field distribution and power

dissipation in the body under investigation. Each human body tissues have a specific permittivity, which is responsible for both electromagnetic field distribution within the human body tissues and heat conversion of that energy. Therefore, the interaction with the electromagnetic fields depends mainly on electric permittivity.

In WBAN, antenna performance operating close to the human body also undergoes near-field losses due to the loss human tissues having conductivity [116] and it causes a decrease in the wearable antenna efficiency [117].

As a result, when an antenna is positioned near lossy human tissues, the frequency response and radiation efficiency is significantly affected.Therefore, a body phantom should be included in the design process.

2.5.2. Reader Antenna Optimization

A circular disc monopole antenna is designed on Rogers RO3210 with a relative permittivity of 10.2 and fed by 50Ω coplanar-waveguide(CPW) as described in [82]. The antenna was modeled to operate on a realistic human model in ANSYS HFSS. The antenna geometry is shown in Figure 2.11, and the optimized values of antenna dimensions are shown in Table 2.3.

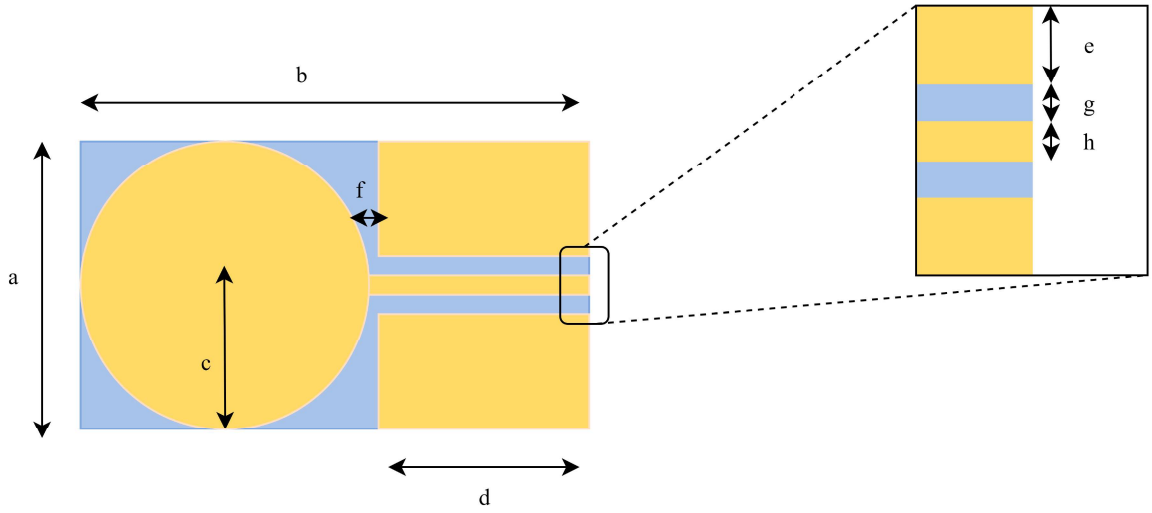

Figure 2.11. The representation of the reader antenna with final values.

The operating bandwidth of the proposed antenna is mainly dependent on the feed gap, width of the ground plane, and the radius of the disc. Also, the relationship between the first resonance frequency and disc radius is shown in Figure 2.7. Therefore, these variables are mainly optimized for optimizing the antenna for on-body operation.

Coplanar waveguide feed structure, as seen in Figure 2.13, is recalculated to obtain 50 Ω input impedance in [118] since a different dielectric substrate is used for the antenna design.

Figure 2.12 shows the sandwiched CPW structure. After all derivations to determine Z_o and Z_o for the sandwiched CPW is adapted to calculate them for conventional CPW on a dielectric substrate of finite thickness, as shown in Figure 2.13.

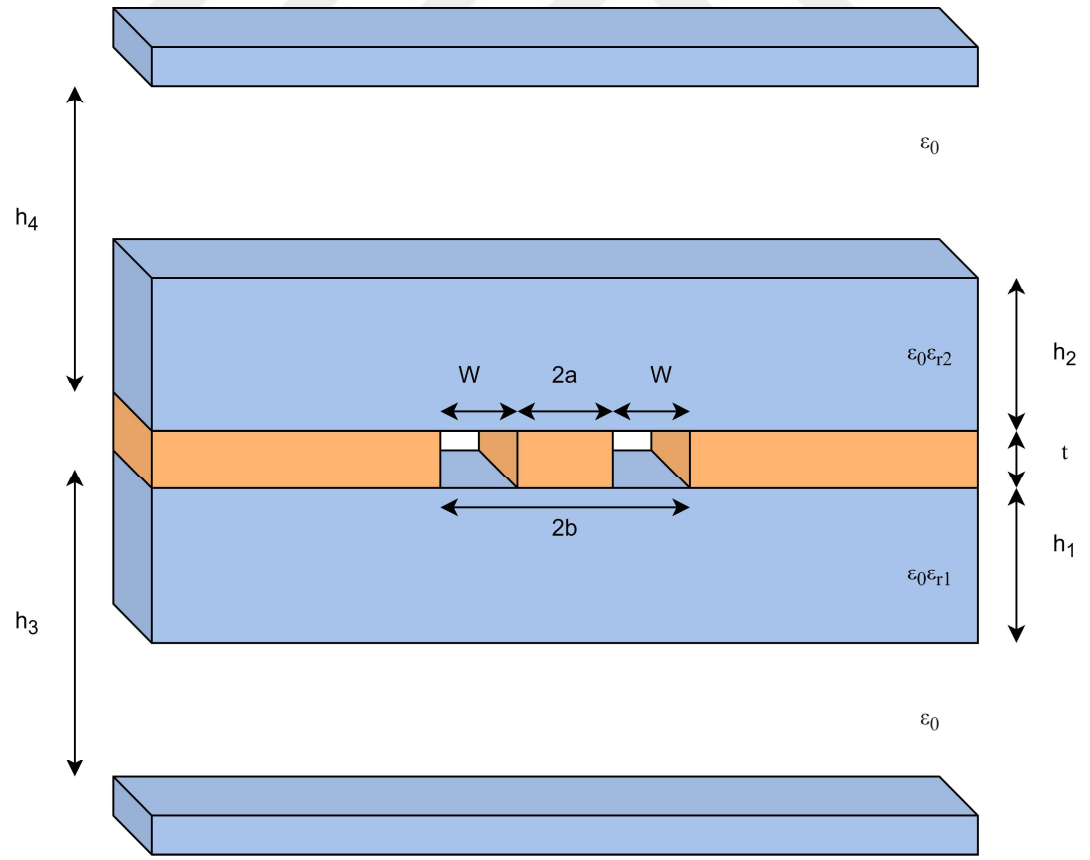

Figure 2.12. The sandwiched CPW structure between two dielectric substrates.

In the following analysis, the CPW conductors and the dielectric substrates are assumed to have perfect conductivity and relative permittivity, respectively. Hence the structure is considered to be lossless. Further, the dielectric substrate materials are considered to be isotropic.

Conformal mapping techniques are presented to express Z_0 and ε_{eff}. It is assumed that the conductor thickness is zero and magnetic walls are present along all dielectric boundaries, including the CPW slots [119]. The CPW is then divided into several regions, and the electric field is assumed to exist only in that partial region.

The total capacitance C_{CPW} is the sum of the partial capacitances C_1, C_2 and C_{air} of the three partial regions shown in Figure 2.12 and expressed as

$$C_{\text{CPW}} = C_1 + C_2 + C_{\text{air}} \tag{2.3}$$

where C_1 and C_2 are the partial capacitance of the CPW with only the lower and upper dielectric layers, respectively. C_{air} is the capacitance of the CPW in the absence of all the dielectric layers. The capacitance C_1 of the lower partial dielectric region is given by

$$C_1 = 2\varepsilon_0(\varepsilon_{\text{r1}} - 1)\frac{K(k_1)}{K(k_1')} \tag{2.4}$$

where $K(k_1)$ and $K(k_1')$ mean the modulus of the complete elliptic integrals and k_1 and $k_1^{'}$ are calculated as

$$k_1 = \frac{\sinh\left(S\pi/4h_1\right)}{\sinh\left[[\pi(S+2W)]/4h_1\right]} \tag{2.5}$$

$$k_1' = \sqrt{1-k_1^2}. \tag{2.6}$$

The capacitance C_2 of the upper partial dielectric region is given by

$$C_2 = 2\varepsilon_0(\varepsilon_{\text{r2}} - 1)\frac{K(k_2)}{K(k_2')} \tag{2.7}$$

where K(k_2) and K(k_2') means the modulus of the complete elliptic integrals and k_2 and $k_2^{'}$ are calculated as

$$k_2 = \frac{\sinh\left(S\pi/4h_2\right)}{\sinh\left[[\pi(S+2W)]/4h_2\right]} \tag{2.8}$$

$$k_2' = \sqrt{1-k_2^2}. \tag{2.9}$$

The capacitance C_{air} is given by

$$C_{\text{air}} = 2\epsilon_0\frac{K(k_3)}{K(k_3')} + 2\epsilon_0\frac{K(k_4)}{K(k_4')} \tag{2.10}$$

where k_3, k_3', k_4 and k_4' are calculated as

$$k_3 = \frac{\tanh\left(S\pi/4h_3\right)}{\tanh\left[[\pi(S+2W)]/4h_3\right]} \tag{2.11}$$

$$k_3' = \sqrt{1-k_3^2} \tag{2.12}$$

$$k_4 = \frac{\tanh\left(S\pi/4h_4\right)}{\tanh\left[[\pi(S+2W)]/4h_4\right]} \tag{2.13}$$

$$k_4' = \sqrt{1-k_4^2}. \tag{2.14}$$

As a result, C_{CPW} is given by

$$C_{\text{CPW}} = 2\varepsilon_0(\varepsilon_{\text{r1}}-1)\frac{K(k_1)}{K(k_1')} + 2\varepsilon_0(\varepsilon_{\text{r2}}-1)\frac{K(k_2)}{K(k_2')} + 2\varepsilon_0\frac{K(k_3)}{K(k_3')} + 2\varepsilon_0\frac{K(k_4)}{K(k_4')}. \tag{2.15}$$

The calculation of the effective dielectric constant, ε_{eff}, phase velocity, υ_{ph} and characteristic impedance, Z_0 is based on the quasi-static approximation and under this approximation, ε_{eff} is defined as

$$\varepsilon_{\text{eff}} = \frac{C_{\text{CPW}}}{C_{\text{air}}}. \tag{2.16}$$

The equivalents of C_{CPW} and C_{air} which were calculated previously are substituted. Then, ε_{eff} becomes as

$$\varepsilon_{eff} = 1 + q_1(\varepsilon_{r1} - 1) + q_2(\varepsilon_{r2} - 1) \tag{2.17}$$

where q_1 and q_2 are called the partial filling factors, and they are expressed as

$$q_1 = \frac{K(k_1)}{K(k_1')}[\frac{K(k_3)}{K(k_3')} + \frac{K(k_4)}{K(k_4')}]^{-1} \tag{2.18}$$

$$q_2 = \frac{K(k_2)}{K(k_2')}[\frac{K(k_3)}{K(k_3')} + \frac{K(k_4)}{K(k_4')}]^{-1}. \tag{2.19}$$

Moreover, the relation between phase velocity, v_{ph} and effective permittivity, ε_{eff}, is defined as

$$v_{ph} = \frac{c}{\sqrt{\varepsilon_{eff}}}. \tag{2.20}$$

where c is the velocity of the light in free space. Also, the relation between phase velocity, v_{ph} and characteristic impedance, Z_0 is expressed as

$$Z_0 = \frac{1}{C_{CPW} v_{ph}}. \tag{2.21}$$

Then, characteristic impedance, Z_0 is calculated as

$$Z_0 = \frac{1}{cC_{air}\sqrt{\varepsilon_e ff}} = [\frac{60\pi}{\sqrt{\varepsilon_e ff}}\frac{K(k_3)}{K(k_3')} + \frac{K(k_4)}{K(k_4')}]^{-1}. \tag{2.22}$$

The structure schematically illustrated in Figure 2.13 shows that ε_{r2} is equal to 1 and h_3 and h_4 approach to ∞. Thus, partial capacitance C_1 and C_2 are recalculated as

$$C_1 = 2\varepsilon_0(\varepsilon_{r1} - 1)\frac{K(k_1)}{K(k_1')} \tag{2.23}$$

$$C_2 = 0. \tag{2.24}$$

Due to the h_3 and h_4 approach to infinity, k_0,k_3 and k_4 are expressed as

$$k_0 = k_3 = k_4 = \frac{S}{S + 2W}. \tag{2.25}$$

Thus, C_{air} is recalculated as follows

$$C_{\text{air}} = 4\varepsilon_0 \frac{K(k_0)}{K(k_0{}')}. \tag{2.26}$$

The recalculated values of C_1,C_2 and C_{air} must be substituted in the total capacitance formula to calculate the total capacitance of the design as shown in Figure 2.13. Thus, the total capacitance C_{CPW} is given by

$$C_{\text{CPW}} = 2\varepsilon_0(\varepsilon_{\text{r1}} - 1)\frac{K(k_1)}{K(k_1')} + 4\varepsilon_0 \frac{K(k_0)}{K(k_0')}. \tag{2.27}$$

In addition, the effective permittivity,ε_{eff}, for the design in Figure 2.13, can be computed as

$$\varepsilon_{\text{eff}} = \frac{C_{\text{CPW}}}{C_{\text{air}}} = 1 + \frac{\varepsilon_{\text{r1}}}{2}\frac{K(k_1)}{K(k_1')} + 4\varepsilon_0 \frac{K(k_0')}{K(k_0)}, \tag{2.28}$$

and the characteristic impedance,Z_0, for the structure in Figure 2.13 can be calculated as follows

$$Z_0 = \frac{1}{cC_{\text{air}}\sqrt{\varepsilon_e f f}} = \frac{30\pi}{\sqrt{\varepsilon_e f f}}\frac{K(k_0')}{K(k_0)}. \tag{2.29}$$

The CPW parameters of the structure seen in Figure 2.13 are calculated by following steps. Thus, trace width (g) and ground spacing (h) become 2.5 mm and 0.8 mm, respectively. The comparison of the first and last case of CPW structures is detailed in Table 2.2. While the input impedance of the CPW structure without ground for the initial design is 55.7 Ω, it is 50.5 Ω for the optimized model.

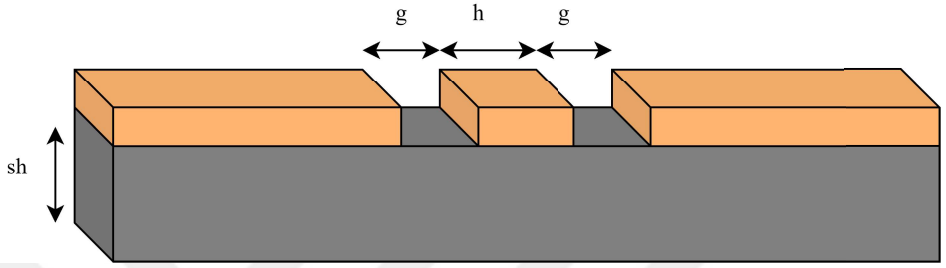

Figure 2.13. The representation of coplanar waveguide structure without ground.

Table 2.2. The coplanar waveguide optimization and xomparison with the initial design.

Substrate Permittivity	**Substrate Height (sh)**	**Ground Spacing (g)**	**Trace Width (h)**	**Z_o**
3	1.6 mm	0.33 mm	4 mm	55.7 Ω
10.2	1.27 mm	0.8 mm	2.5 mm	50.52 Ω

As a result, after feeding mechanism optimization, the final dimensions of the optimized model for the on-body reader antenna are tabulated in Table 2.3. Accordingly, a, b, c, d, e, f, g, and h are 30 mm, 58 mm, 15 mm, 25 mm, 12.95 mm, 0.3 mm, 0.8 mm and 2.5 mm, respectively.

Table 2.3. The optimized values of the reader antenna dimensions.

Antenna Dimension	**a**	**b**	**c**	**d**	**e**	**f**	**g**	**h**
Value (mm)	30	58	15	25	12.95	0.3	0.8	2.5

Figure 2.14 presents the resonance frequencies and the magnitude of the reflection coefficients of the on-body reader antenna on the realistic human model in ANSYS HFSS.

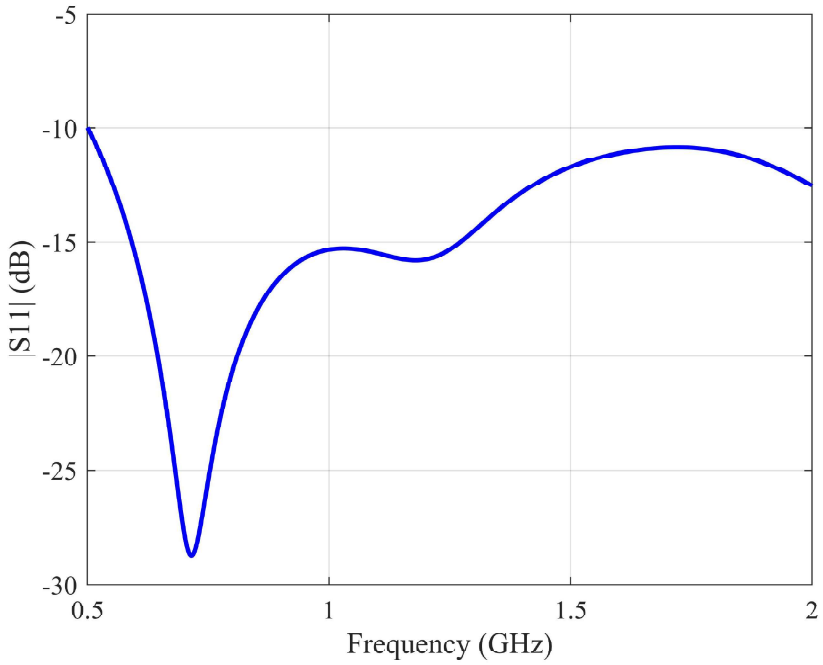

Figure 2.14. The frequency response of the on-body reader antenna.

3. NUMERICAL RESULTS

3.1. Simplification of the Simulation Model

There are many organs and bones such as liver, lung, trachea or scapulain in the realistic human model in ANSYS HFSS as shown in Figure 3.1. They pose different and wide range of electrical characteristics. This complexity significantly affects the simulation time and computational cost. Then, this simplification helps extend the degradation analysis for different human average layer depths between the sternum and the body surface. Thus, the realistic human model has been simplified while preserving the details that would affect the simulation results. These parameters are:

- Electrical characteristic of the human body
- Total dimensions of the human body
- Sternum dimensions such as height and radius
- Distance between the sternum and the body surface

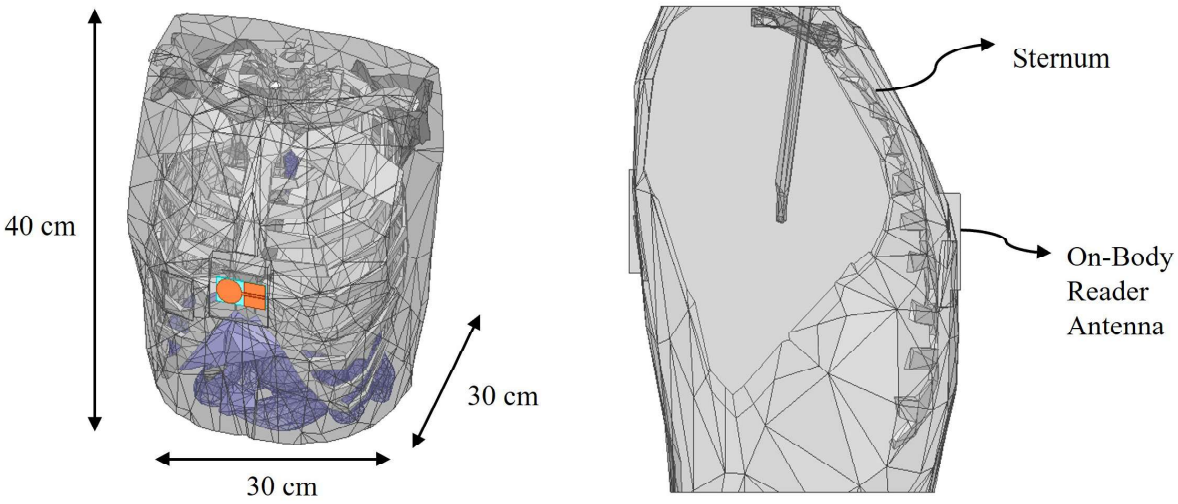

Figure 3.1. The realistic human model with sizes in ANSYS HFSS.

Firstly, a 30 cm x 30 cm x 40 cm box and a cylinder are chosen to represent the human torso and a cylinder is chosen for the human bone, respectively. For the electrical characteristics of the box and the cylinder, “human average” with the relative

permittivity of 31 and conductivity of 0.8 S/m at 1 GHz and “human bone” with the relative permittivity of 16.47 and conductivity of 0.25 S/m at 1 GHz are assigned in ANSYS HFSS, respectively.

The frequency-dependent relative permittivity and conductivity characteristics of the human average material up to 10 GHz are demonstrated in Figure 3.2, while shows the frequency-dependent relative permittivity and conductivity characteristics of the human bone up to 6 Ghz is shown in Figure 3.3.

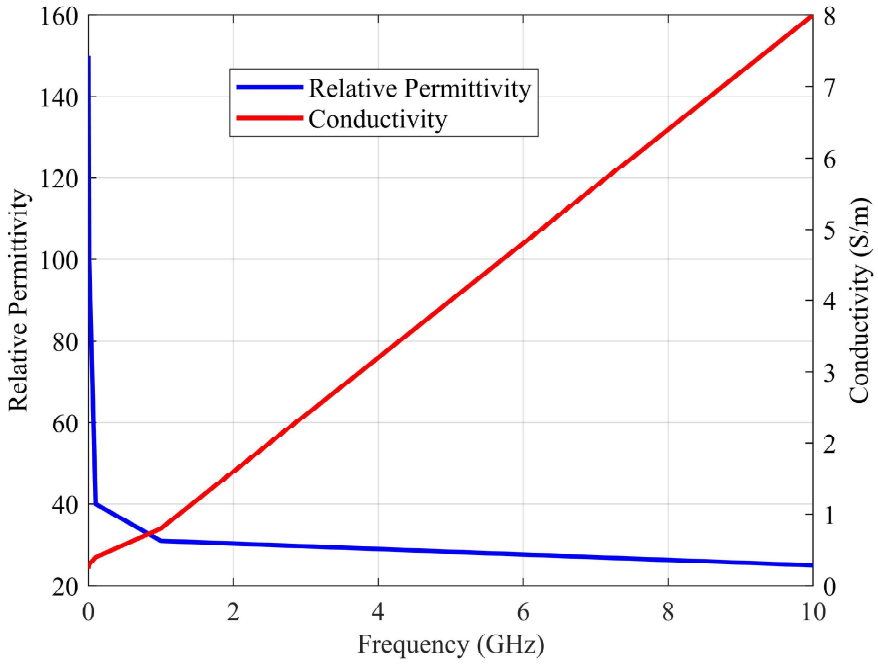

Figure 3.2. The frequency-dependent relative permittivity and conductivity characteristics of human average material in ANSYS HFSS.

In the simplification of the realistic model, the size of the human average box is designed by conversing the total dimensions of the human torso. Also, the distance between the sternum and the body surface is about 25 mm for different locations on the sternum, as shown in Figure 3.4. Therefore, this value is maintained in the simplified model.

Then, as mentioned before, a cylinder is selected to represent the sternum and the radius and height of the cylinder are determined relative to the realistic model, as shown in Figure 3.5.

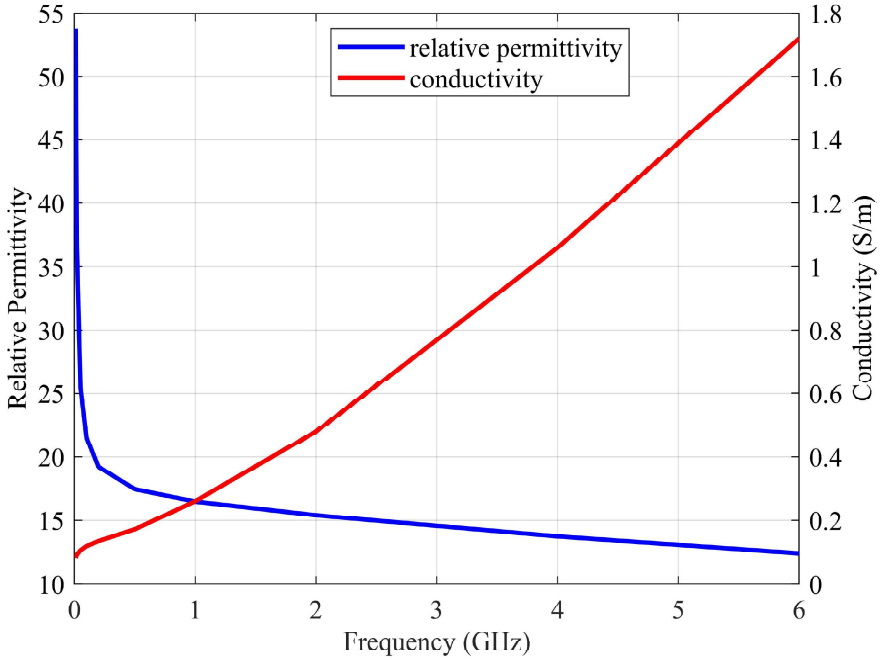

Figure 3.3. The frequency-dependent relative permittivity and conductivity characteristics of human bone material in ANSYS HFSS.

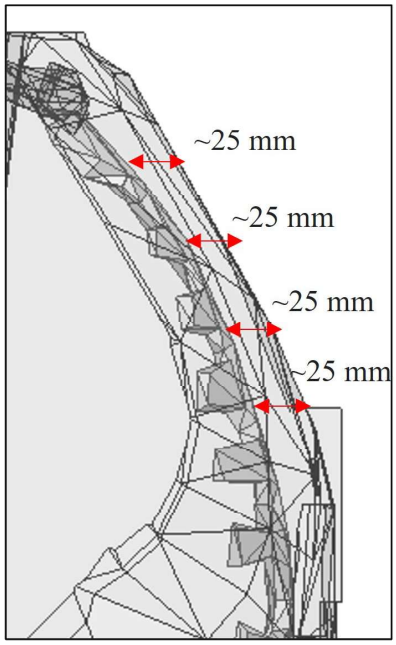

Figure 3.4. The positions of the on-body reader antenna and the sternum.

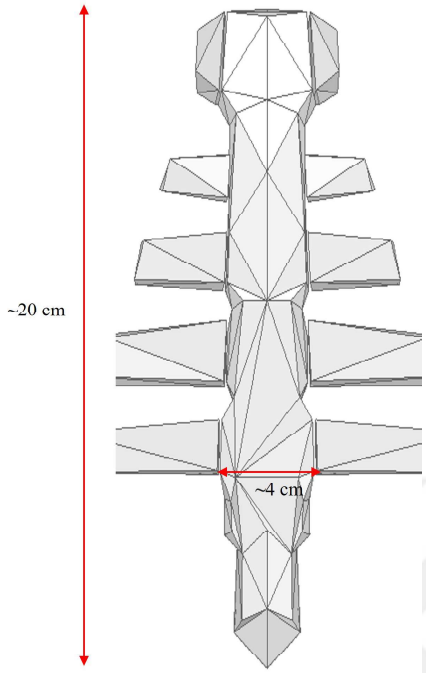

Figure 3.5. The sizes of the sternum.

As a result, the new human torso model and the position of the on-body reader antenna are demonstrated in Figure 3.6, including all the simplifications to the realistic human torso and the sternum.

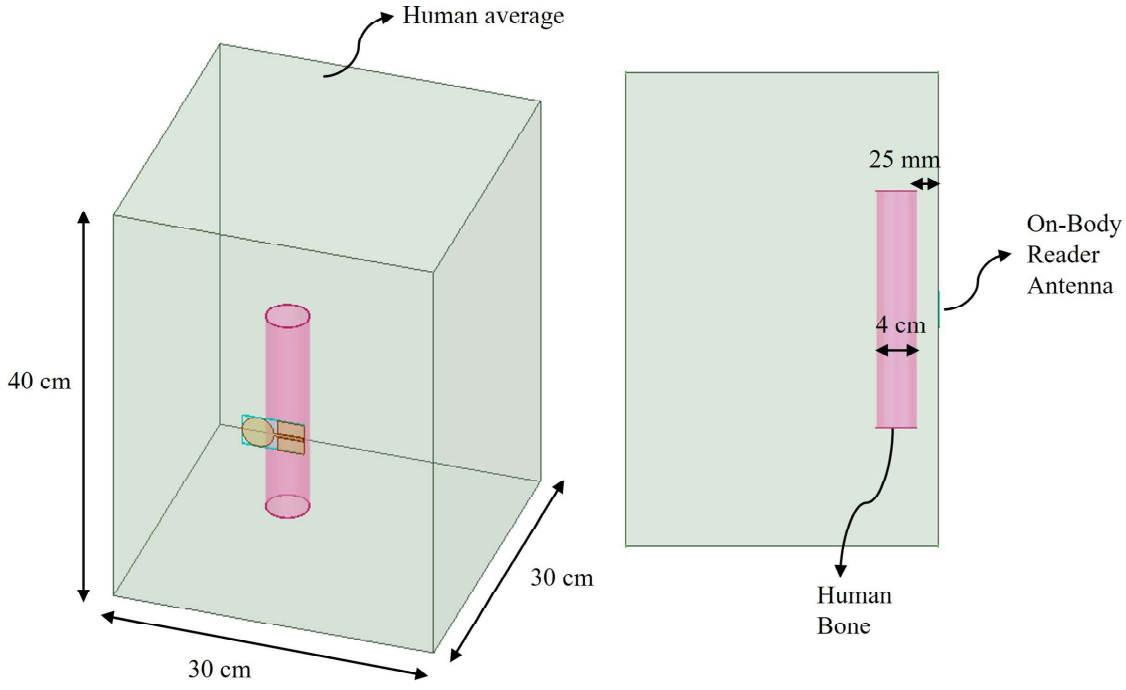

Figure 3.6. The simplified human model relative to the realistic human model.

The reflection coefficient of the on-body reader antenna on the realistic and the simplified human torso model are compared in Figure 3.7 and first resonance frequencies of the on-body reader antenna on both models are detailed in Table 3.1. It can be seen that the first resonant frequency of the reader antenna is 0.71 GHz on the realistic human torso model and 0.72 GHz on the simplified model. This is to ensure that the simplified human torso model case is a good model for the following analyses. It is realized that the change in the reflection coefficient is minimal.

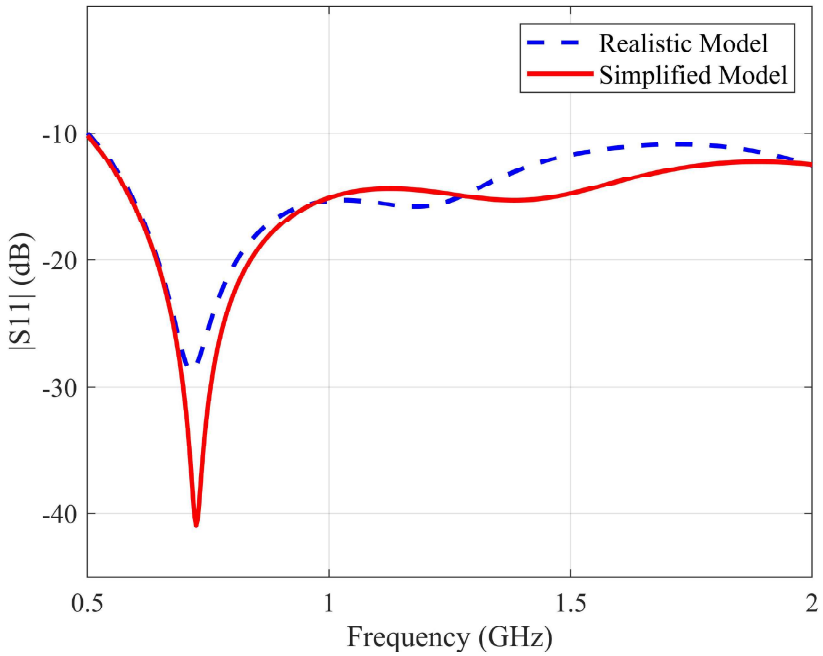

Figure 3.7. The reflection coefficients of the on-body reader antenna on the realistic and simplified human torso model.

Table 3.1. The first resonance frequency and magnitude of return loss of the reader antenna on the realistic and the simplified model.

	Frequency	**dB**
Realistic Model	0.71	28.72
Simplified Model	0.72	40.95

The 3D radiation patterns of the on-body reader antenna on both models at the first resonant frequency are shown in Figure 3.8. The maximum gain is -16.3 dB for the realistic model, while the maximum gain is -14.5 dB for the simplified model. Also, The 2D radiation patterns of the antenna on two models at $\phi = 0°$ and $\phi = 90°$ are given in Figure 3.8. It can be observed that maximum radiation directions stay the same. The half power beamwidths are 100°, 87° and the maximum gain values are -16.3 dB and -14.5 dB for the realistic and the simplified phantom cases, respectively.

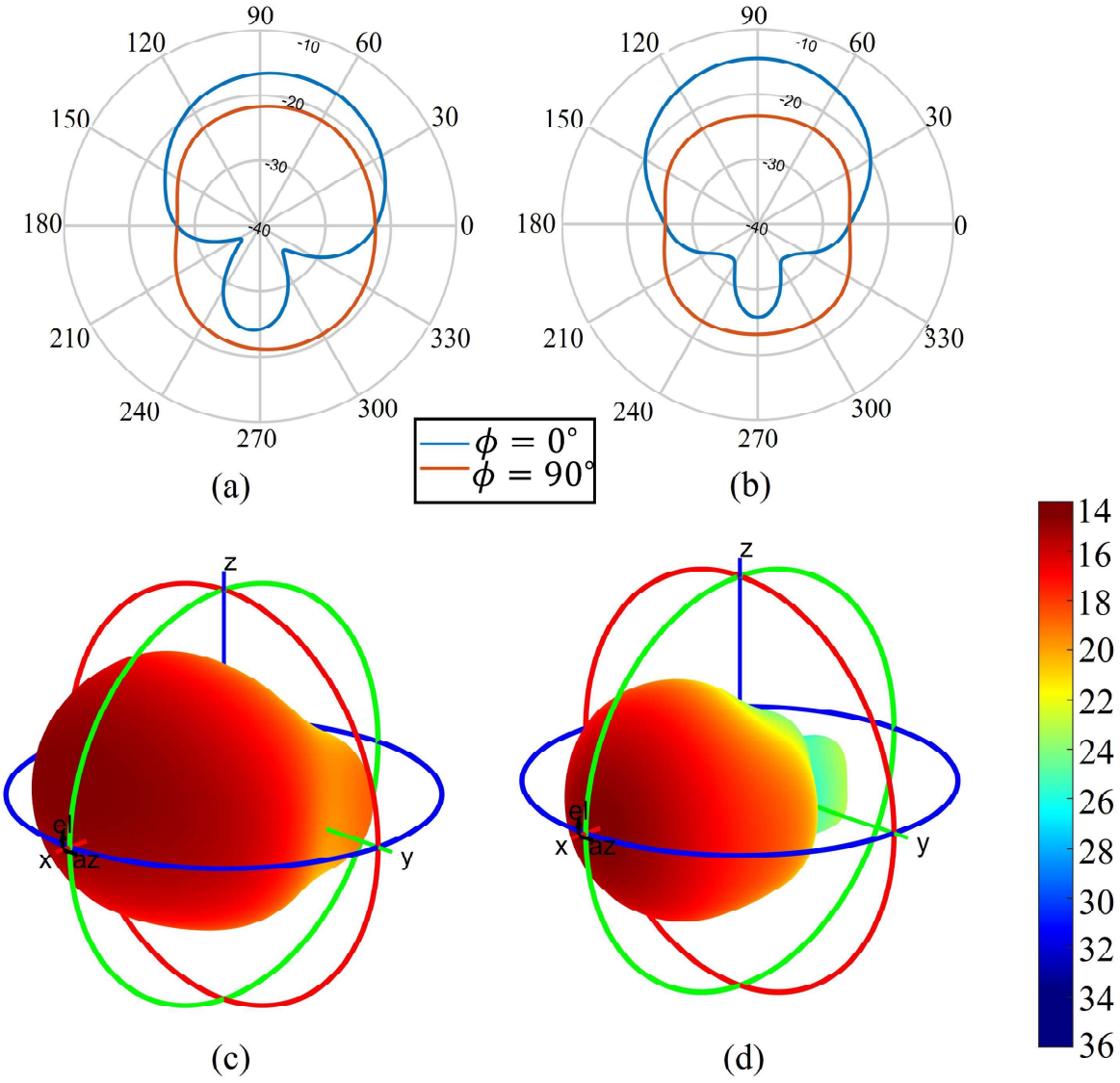

Figure 3.8. The simulated 3D radiation patterns and the corresponding 2D patterns of the on-body reader antenna at $\phi = 0°$ and $\phi = 90°$ on the realistic (left) and simplified (right) human torso model.

3.2. Bone Effect Analysis

As mentioned in Section 3.1, the sternum length and width are about 20 cm and 40 mm, respectively. Although these are generally constant along with adulthood, they can vary slightly from person to person. Therefore, the bone effect on the following analyses should be analyzed. Different values are selected for the two criteria and the changes on the reflection coefficient of the on-body reader antenna caused by them are examined. For this purpose, 15 cm, 17 cm, and 20 cm are chosen for the sternum length, and 32 mm, 36 mm, and 40 mm are chosen for the sternum width. Finally, all combinations of these parameters are analyzed. The changes in reflection coefficients are shown in Figure 3.9. As a result, the maximum change in magnitude of return loss and frequency are observed as 2.5 dB and 10 MHz, respectively.

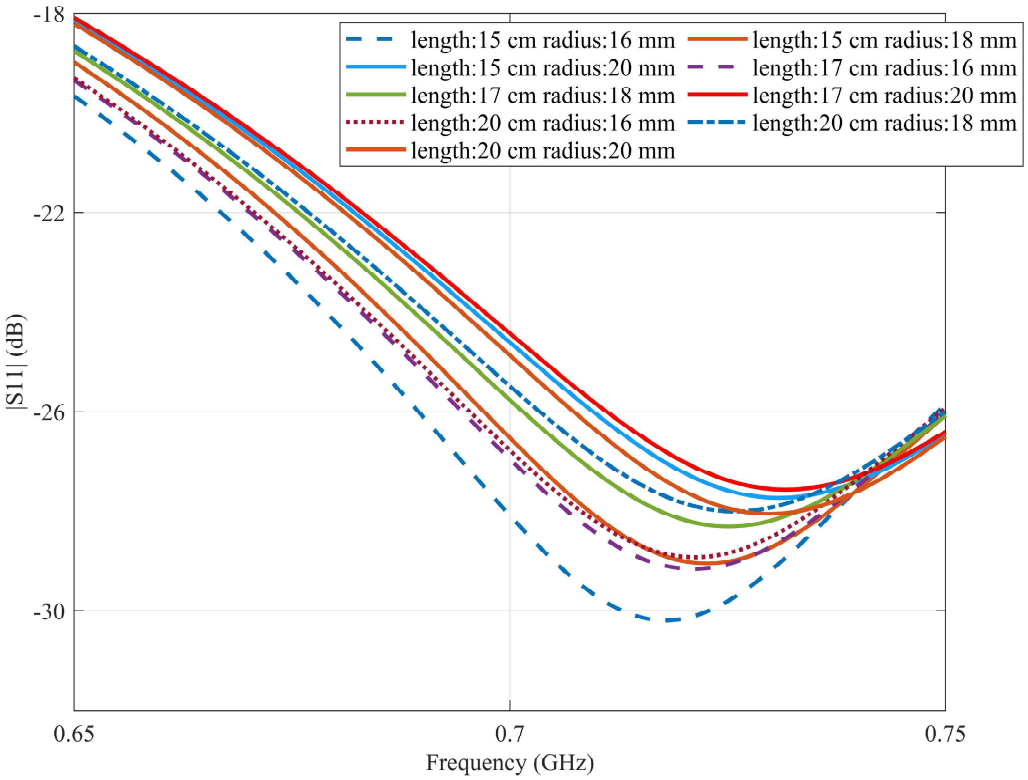

Figure 3.9. The frequency response of only human bone with different length and width variations.

3.3. Degradation Analysis of only One Magnesium Suture

The changes in the structure of the metallic sutures affect the reflection characteristics of the on-body reader antenna. As the Mg suture degrades, a shift in the resonant frequency of the reader antenna will be observed. The magnesium suture surrounding the sternum horizontally is modeled as a metal loop with a radius of 20 mm. The loop has a square cross-section with a side length of 1 mm. Fig. 3.10 presents the change in the reflection coefficient of the reader antenna as the suture degrades. It can be seen that the resonant frequency of the on-body antenna shifts from 0.73 GHz (-28.14 dB) to 0.715 GHz (-39.82 dB) for 25 mm suture depth, as tabulated in Table 3.2.

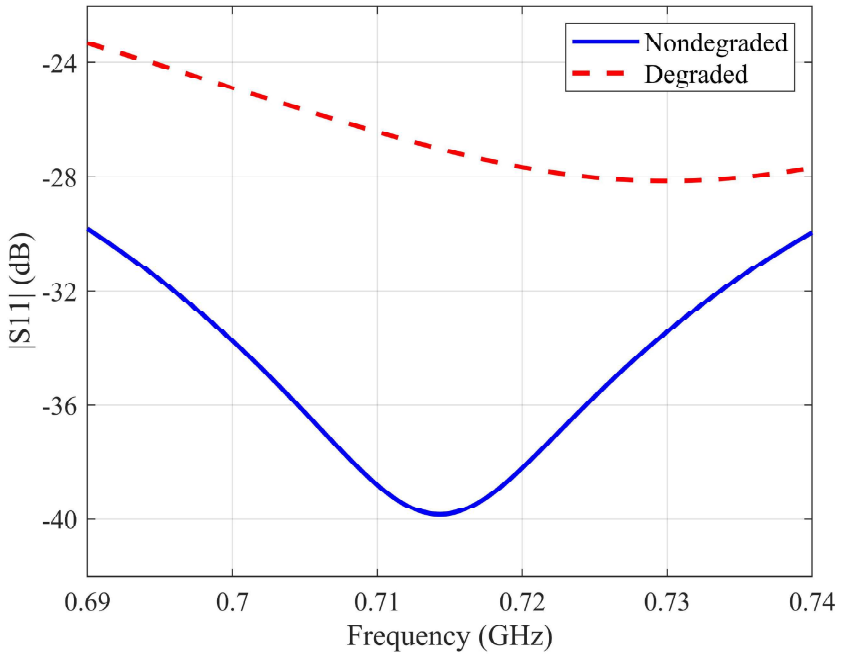

Figure 3.10. The change in reflection coefficient in the degradation process.

Table 3.2. The resonant frequency and the magnitude of return loss of the degraded and nondegraded cases of the magnesium suture.

	Frequency (MHz)	**dB**
Nondegraded	0.715	39.82
Degraded	0.73	28.14

Also, the electric field distribution on magnesium suture at the resonant frequency is simulated to analyze the breakage point on magnesium suture and is demonstrated in Figure 3.11.

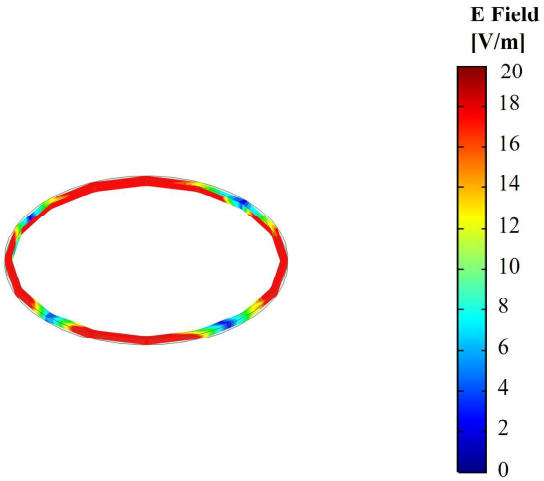

Figure 3.11. The electric field distribution of Mg-based suture at the resonance frequency.

3.4. Breakage Point Analysis

The suture can fail to maintain its integrity in the postoperative healing and this case can cause serious problems. Therefore, the detection of breakage on the Mg suture becomes an important point. To model this effect, a 1mm $\times$ 1mm piece is removed from the Mg suture suture as shown in Figure 3.12. Then, the breakage is moved along the suture with a rotation angle, ϕ with a step of 20°. In the following periods, the breakage point analysis is simulated at each 20° after the starting point.

Figure 3.14 shows the change in reflection coefficients for different breakage positions on magnesium suture. Finally, none of the reflection coefficient plots intersect with the degraded and nondegraded results mentioned in the previous section. Thus, it is anticipated to be detected whether there is a breakage on the magnesium suture.

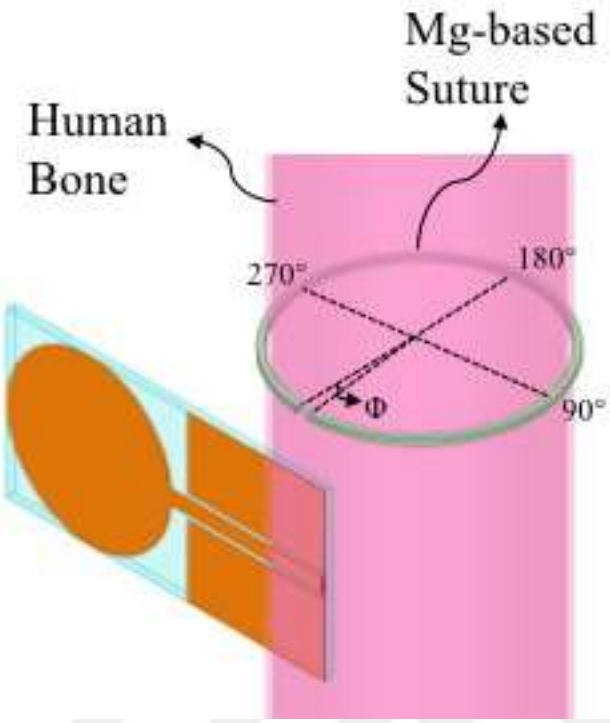

Figure 3.12. The representation of different breakage points on magnesium suture and the location of the reader antenna

Also, the electric field distribution on magnesium suture caused by breakage at 0°, 90°, 180°, and 270° is demonstrated in Figure 3.13.

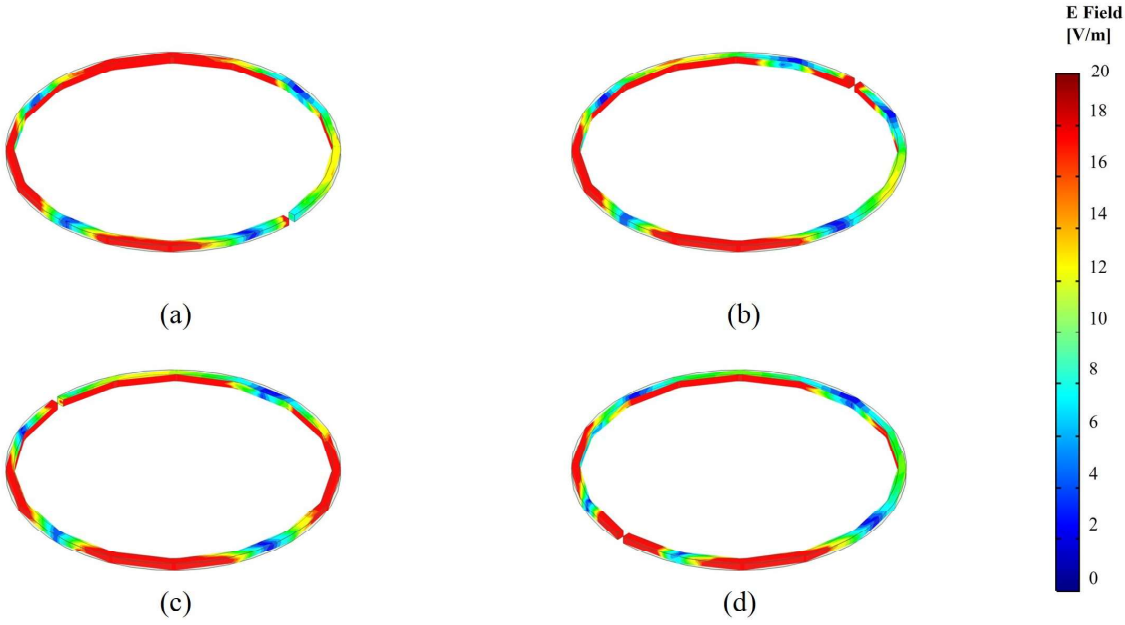

Figure 3.13. The electric field distribution on magnesium suture caused by breakage at 90° (a), 180° (b), 270° (c), 0° (d).

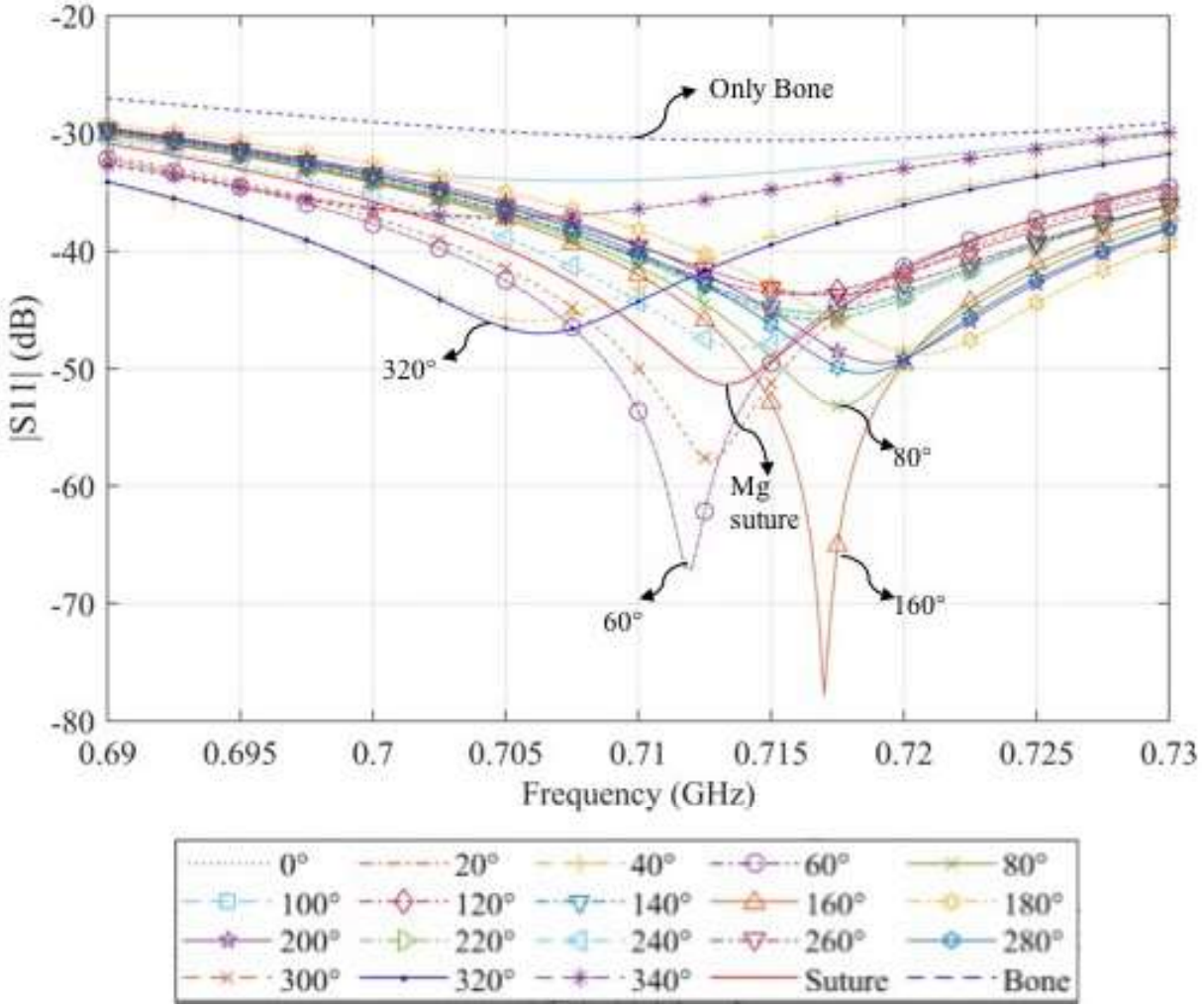

Figure 3.14. The reflection coefficients of the reader antenna caused by different locations of breakage on Mg suture

3.5. Degradation Analysis for Different Human Average Depths

The degradation analysis in Section 3.2 is carried out by taking the thickness human average layer as 25 mm. To represent the cases of underweight, overweight and average weight people, the thickness of the human average layer between the on-body reader antenna and Mg-based suture in the numerical model is increased from 15 mm to 30 mm as shown in Figure 3.15.

Figure 3.16 shows the change in reflection coefficients of the reader antenna along with the degradation of magnesium suture on the bone for different depths.

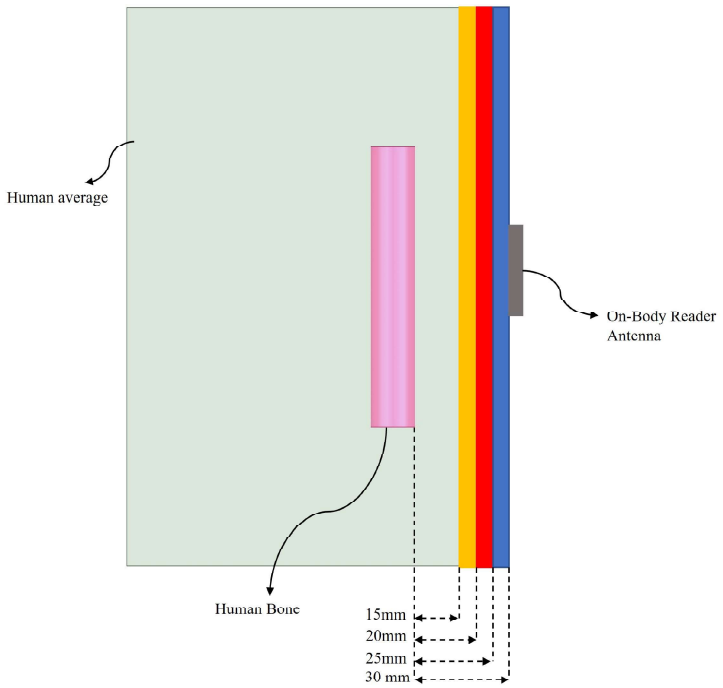

Figure 3.15. The representation of the different human average layer depths between the Mg suture and the reader antenna

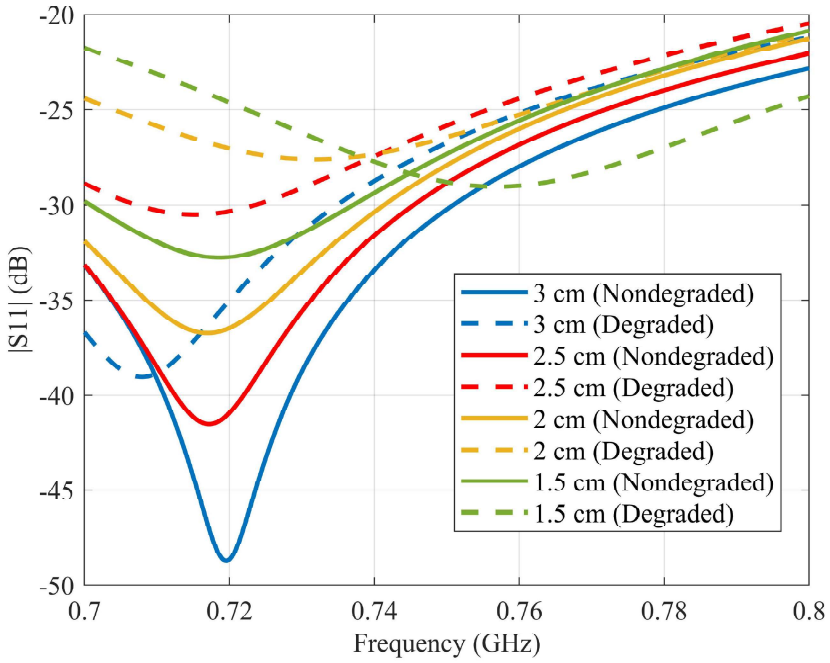

Figure 3.16. The frequency response of the degraded (dash line) and nondegraded (line) Mg suture in the different human average phantom thicknesses.

3.6. Misalignment of the Mg Suture and the Reader Antenna

In Section 3.3, the tracking of Mg suture degradation relies on the alignment of the on-body reader antenna and the Mg suture. In this section, the sensitivity of the tracking on the misalignment is analyzed by changing the suture position as seen in Fig. 3.17.

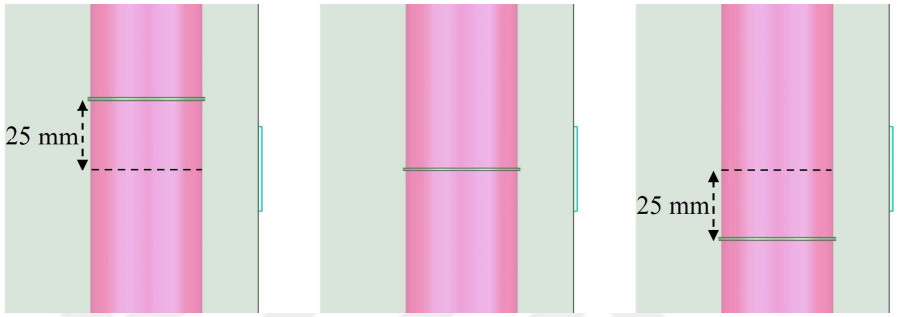

Figure 3.17. The representation of the different positions of the magnesium suture on the human bone.

Figure 3.18 shows the change in reflection coefficients of the reader antenna along with the degradation of the magnesium suture at the different positions on the bone.

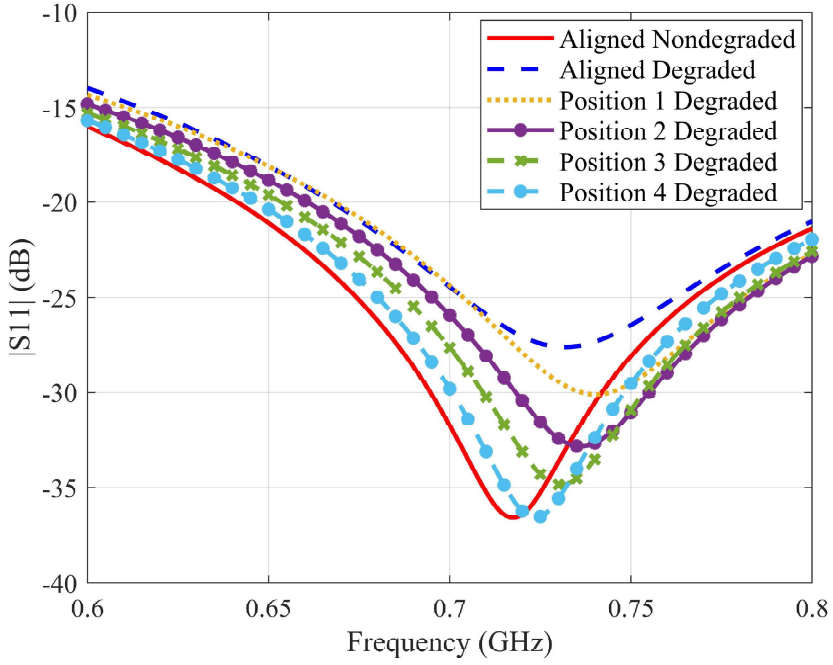

Figure 3.18. The frequency response of the different positions of the magnesium-based suture relative to the reader antenna.

4. MEASUREMENT RESULTS

4.1. Antenna Prototyping

The reader antenna is prototyped using single layer of 1.27 mm Rogers RO3210 dielectric substrate. The fabrication is made with Leiterplatten-Kopierfräsen (LPKF) S103. The refection coefficient of the prototyped antenna is measured using PICO VNA106 which is calibrated in 0.5-2 GHz frequency band. Figure 4.1 shows the completed prototype of antenna.

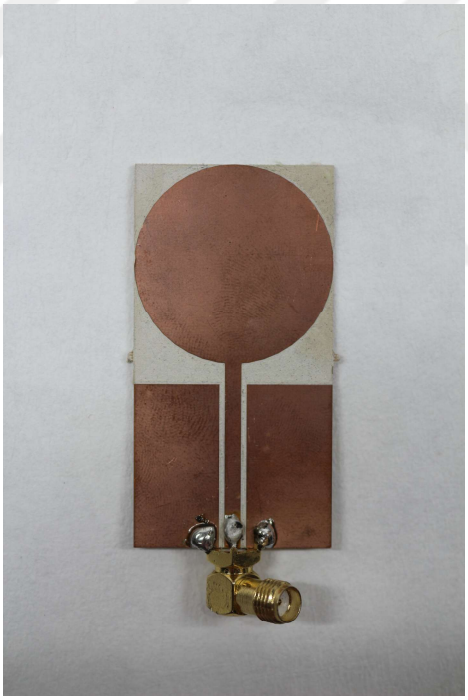

Figure 4.1. The prototyped on-body reader antenna.

Figure 4.2 shows the simulated and measured reflection coefficients of the optimized on-body reader antenna for the operation on human average phantom. Also, the first resonance frequencies and the magnitude of the reflection coefficients of the reader antenna are tabulated in Table 4.1.

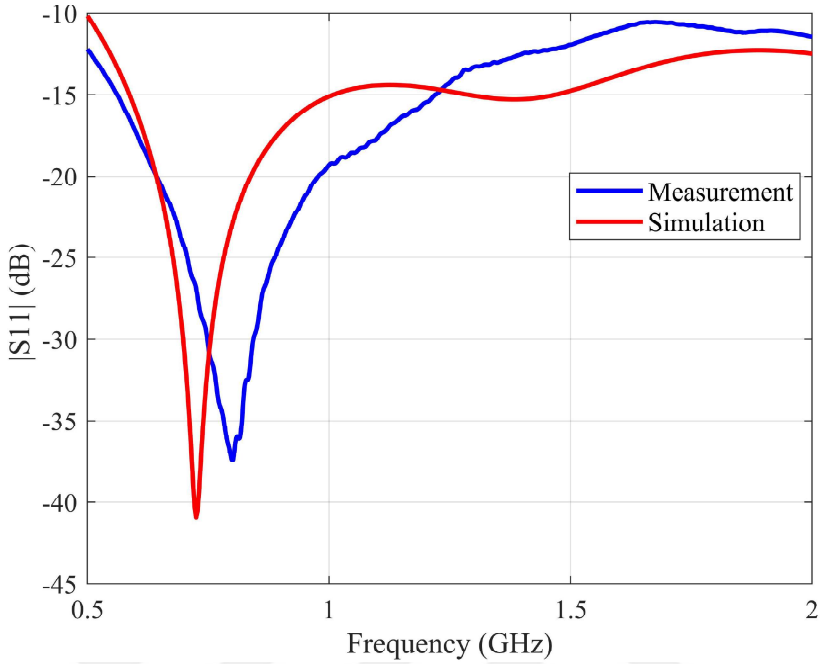

Figure 4.2. The reflection coefficients of the reader antenna on the human average phantom for simulation and measurement model.

Table 4.1. The first resonance frequency and the magnitude of the reflection coefficients of the reader antenna on the simulation and measurement model.

	Frequency (MHz)	**dB**
Simulation	725	-40.95
Measurement	814	-36.1

4.2. Fabrication of the Measurement Setup

4.2.1. Phantoms

The human body has intense electrical properties, and these make the human body a lossy environment for electromagnetic radiation. Therefore, it is fundamental that a device's performance is established during the development process when it interacts electromagnetically with the human body [120]. Phantoms are typically chemical structures that mimic the electrical characteristics of human tissues [121].

Thus, they are widely utilized in measurement set-ups developed to accurately evaluate antenna performance distortions caused by the vicinity of the human body [122]. The phantoms have been classified in many different ways. Firstly, they can be classified in terms of their final forms as solid phantoms [123], semi-solid phantoms [124], or liquid phantoms [125]. Also, the main material in the production process can be used for classification, such as water-based phantoms [125], oil-in-gelatine phantoms [126], Triton X100 phantoms [127], and 3D printed phantoms [128]. Finally, phantoms can be grouped based on the part of the body they mimic, such as head phantoms [124], hip phantoms [125], or breast phantoms [129].

4.2.2. Fabrication of Human Average and Human Bone Phantoms

The tissue-mimicking mixtures are water-based, semi-solid mixtures prepared using distilled water, oil, dish detergent, and cornstarch. The two electrical properties replicated by the mixtures are the relative permittivity and conductivity.

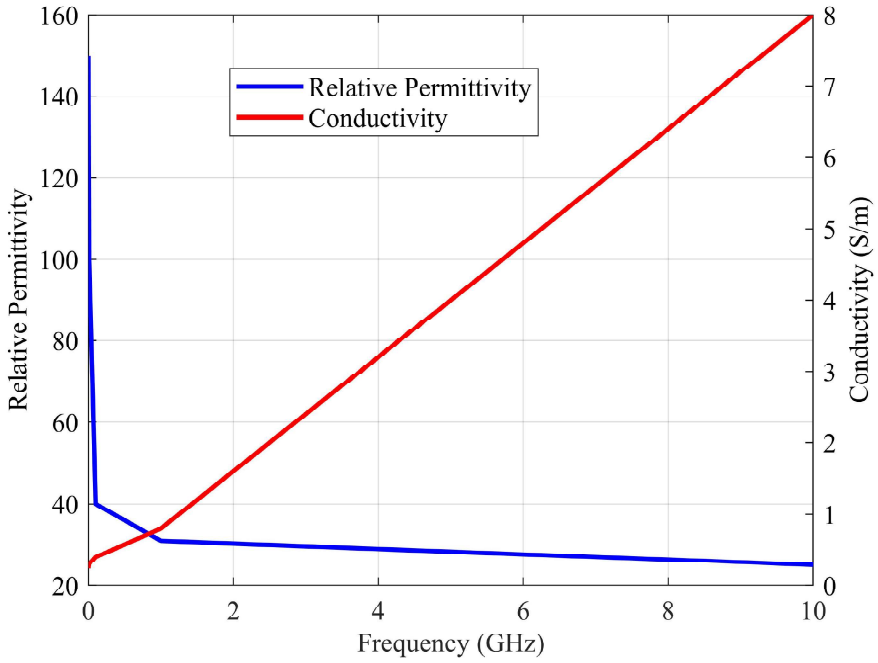

Figure 4.3. The frequency-dependent relative permittivity and conductivity values of the human average in ANSYS HFSS.

Table 4.2. The electrical properties of the human average tissue at 1 GHz in ANSYS HFSS.

	Human Average
Relative Permittivity	31
Conductivity (S/m)	0.8

The frequency-dependent relative permittivity and conductivity values of human average obtained from ANSYS HFSS are shown in Figure 4.3 and tabulated in Table 4.2 for 1 GHz. The quantity of each ingredient required to prepare the mixtures is provided in Table 4.3.

Table 4.3. The quantity of each ingredient required for the human average phantom

Ingredients	**Human average**
Distilled Water	2 L
Oil	1 L
Dish Detergent	1 L
Cornstarch	600 gr

Table 4.4. The electrical properties of the human bone at 1 GHz.

	Human Bone
Relative Permittivity	16.47
Conductivity (S/m)	0.26

The frequency-dependent relative permittivity and conductivity values of human bone are shown in Figure 4.4 and tabulated in Table 4.4 for 1 GHz. The quantity of each ingredient required to prepare the mixture is provided in Table 4.5.

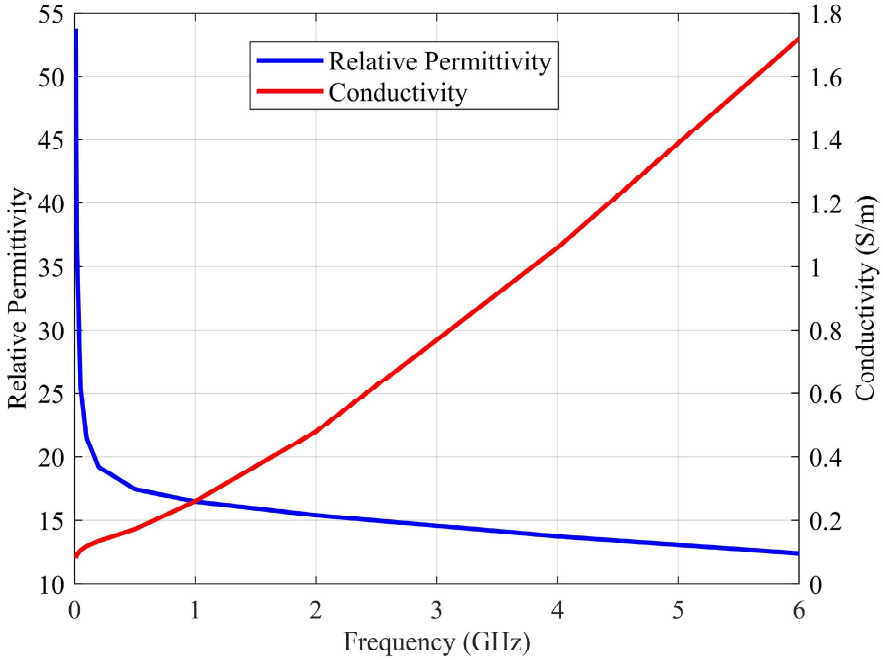

Figure 4.4. The frequency-dependent relative permittivity and conductivity values of the human bone in ANSYS HFSS.

Table 4.5. The quantity of each ingredient required for human bone phantom.

Ingredients	**Human Bone**
Distilled Water	300 ml
Oil	100 ml
Dish Detergent	100 ml
Cornstarch	1000 gr

The procedure to be followed for the fabrication of the tissue-mimicking human average and human bone phantom is as follows:

- Step 1: Distilled water, oil, and dish detergent are put into a beaker. Then, the beaker is placed on a hot plate. The mixture is heated gradually to 80°. At the same time, the mixture should be regularly stirred via a magnetic stirrer to obtain a homogeneous, high-viscosity mixture.
- Step 2: When the temperature reaches 40°, cornstarch is poured by continuously stirring in small portions. It is necessary to ensure that the cornstarch does not form a precipitate at the bottom of the beaker and that it dissolves homogeneously in the mixture. Using sieve for adding cornstarch make this process easier.
- Step 3: At 80°, there will be an increase in the viscosity of the mixture. At this stage, the heating is stopped.
- Step 4: With the increase in viscosity, additional cornstarch is added to the mixture to determine the final permittivity value.
- Step 5: Finally, the mixture is allowed to cool at room temperature while stirring via a magnetic stirrer.

As water has high permittivity, it is the main source of permittivity in the mixture. Cornstarch has two critical missions in tissue-mimicking mixtures. The cornstarch added in the heating process is used to tune the viscosity of the phantom. Also, in the cooling process, the cornstarch is used to decrease the permittivity of the mixture. In other words, it is a material to control the final permittivity value. Also, salt can be used to control the final value of conductivity. However, it should be dissolved with water and added to the mixture instead of adding salt directly to the mixture.

The given fabrication process of tissue mimicking mixture is demonstrated in Figure 4.5.

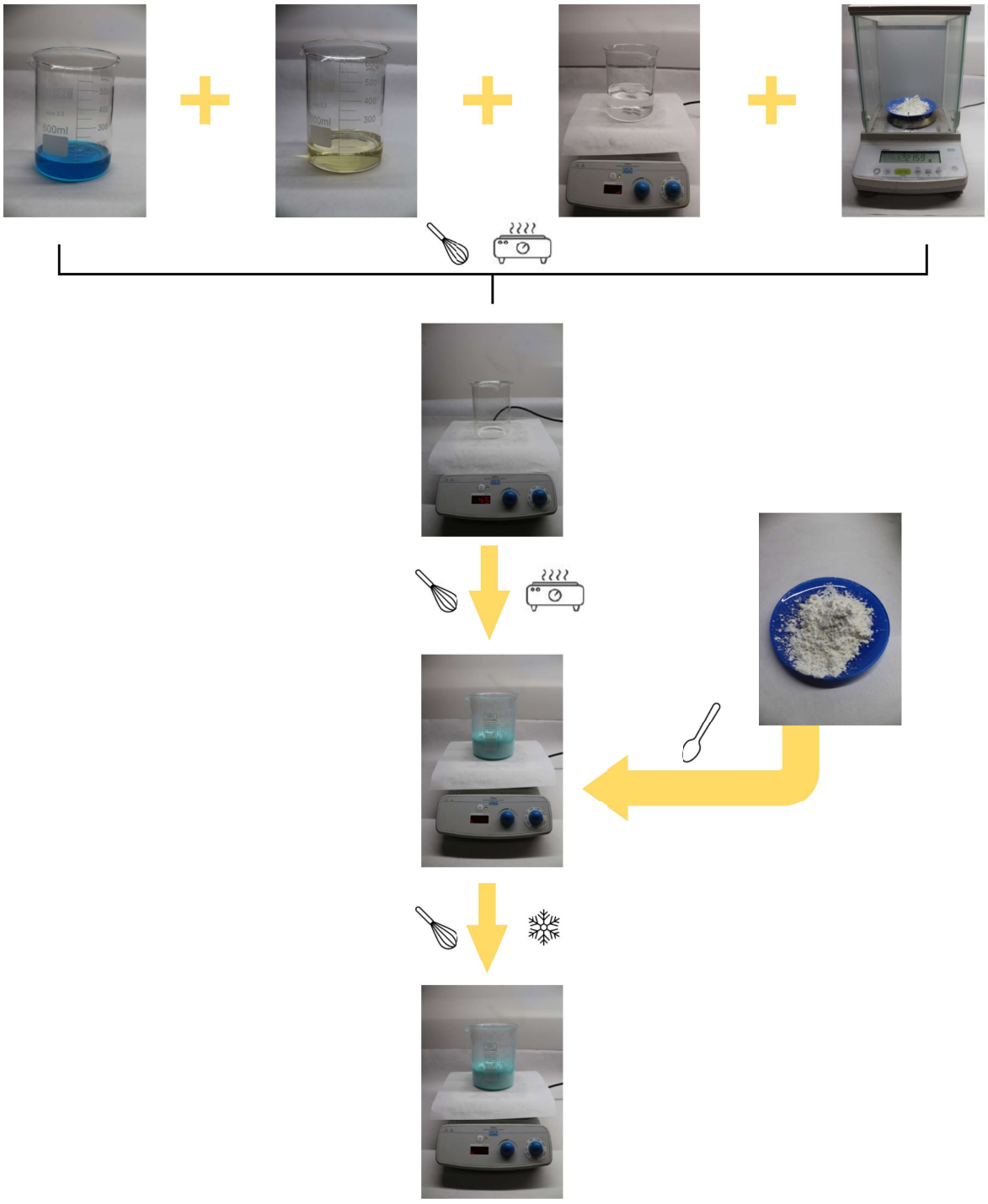

Figure 4.5. The fabrication process of tissue-mimicking human average and human bone phantom.

4.2.3. Measurement of the Electrical Properties

The electrical characteristics of the tissue-mimicking human average and human bone phantom are measured in a wide frequency range by using the Speag Dielectric Assessment Kit (DAK) in Figure 4.6.

Figure 4.6. The Speag DAK probe station.

In the DAK, an open-ended coaxial cable in the test medium is used as the probe. The open ended coaxial is a cut-off section of 50 Ω transmission line. The fringing electric fields inside the medium at the end of the cable are modeled using a virtual transmission line length; that is, the coaxial cable is assumed to enlarge inside the test medium [130]. The permittivity of the test medium is determined from the change of the reflection coefficient [130]. Note that the material is measured either by touching the probe to the surface of a solid or by immersing it into a liquid media. Also, the relative permittivity of the test medium is taken as the relative permittivity of the virtual transmission line [130].

The dielectric parameters of liquids are usually frequency and temperature dependent. Therefore, samples must be homogeneous, isotropic and sufficiently large and should be measured at a stable temperature. Note that it is also important to validate the measurement by using a well-characterized reference liquid such as ethanol or methanol.

The complex permittivity of a homogeneous, isotropic and free of impurities medium is a complex quantity that depends on both the relative permittivity and the conductivity of the medium [130] and given as

$$\varepsilon^* = (\varepsilon'/\varepsilon_0) - j(\varepsilon''/\varepsilon_0), \tag{4.1}$$

$$\sigma = 2\pi f \varepsilon'' \varepsilon_0, \tag{4.2}$$

$$\tan(\delta) = \frac{\varepsilon''}{\varepsilon'} \tag{4.3}$$

where ε_0 is the permittivity of free space and equal to 8.854 pF/m. Also, the relative permittivity is the real part of the complex permittivity, as shown above.

Figure 4.8 and Figure 4.9 show the permittivity and conductivity values along with the frequency for the human average and human bone phantom, respectively.

Furthermore, an empty cylindrical model with 0.5 mm wall thickness, as seen in Figure 4.10, is printed using Formlabs 3B SLA 3D printer to fill the human bone phantom. Formlabs clear resin is chosen as a substrate, and the electrical characteristics of the clear resin are illustrated in Figure 4.7.

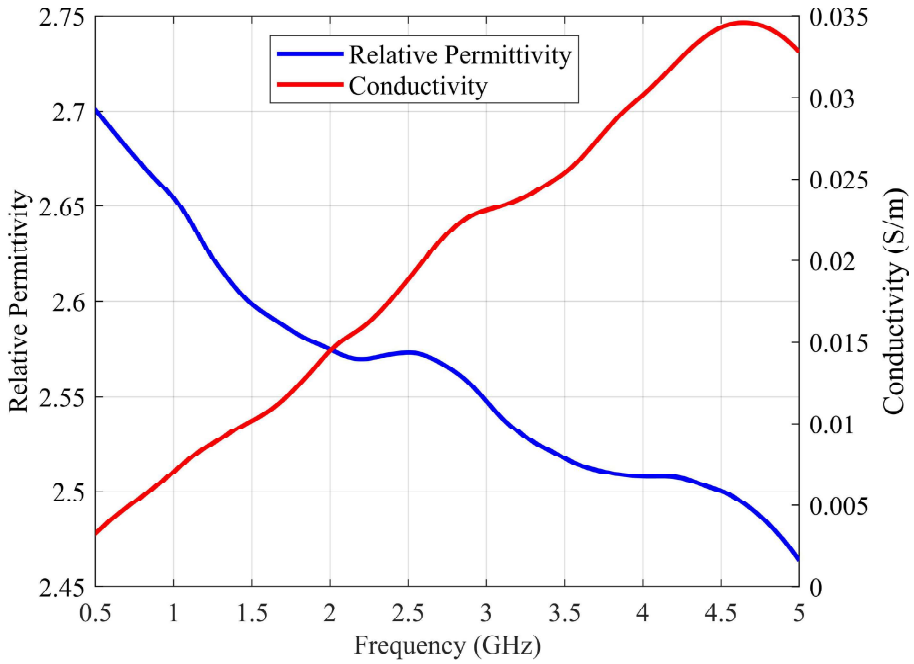

Figure 4.7. The frequency-dependent permittivity and conductivity values of the Formlabs clear resin.

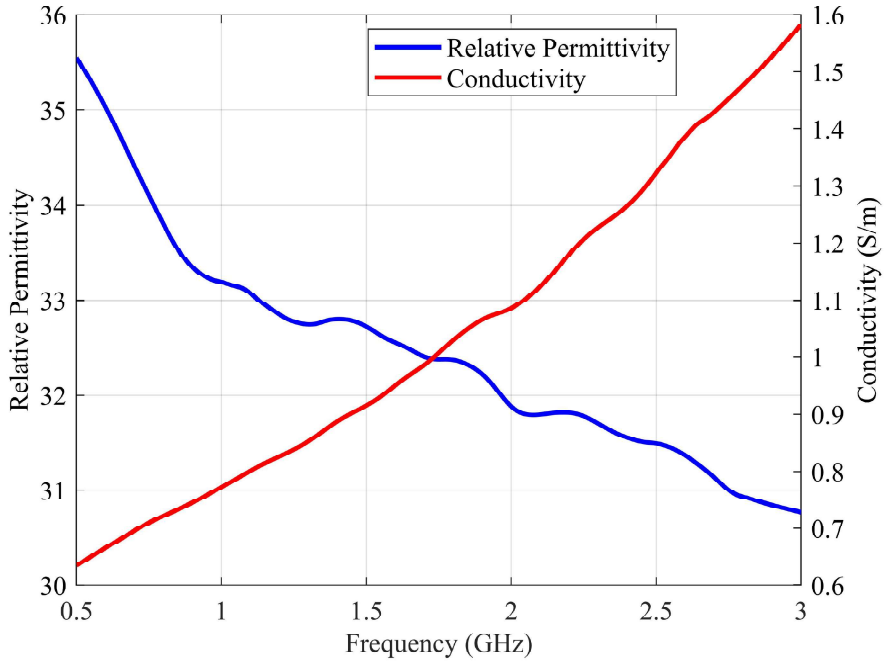

Figure 4.8. The frequency-dependent permittivity and conductivity values of the tissue-mimicking human average phantom.

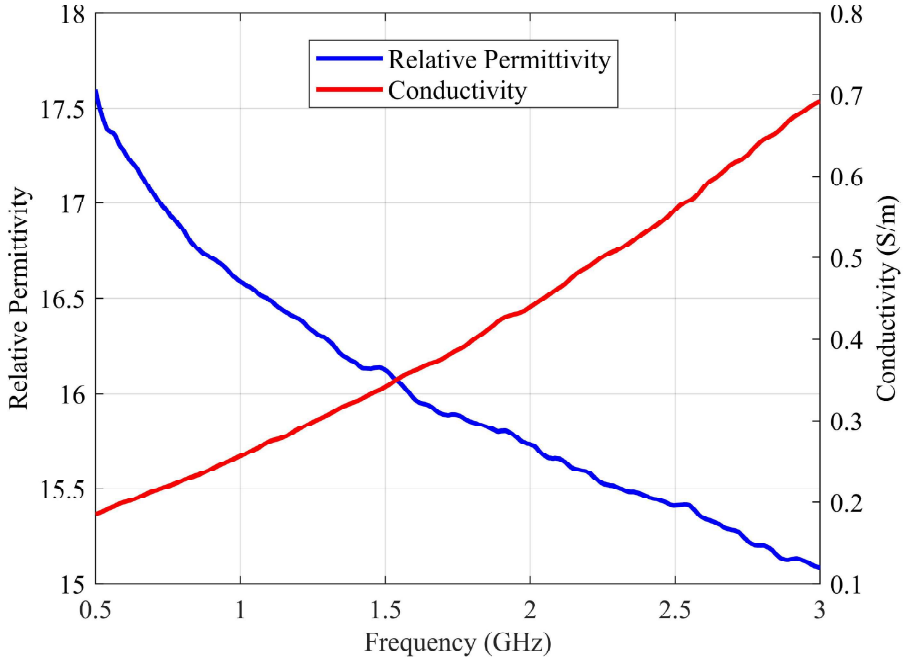

Figure 4.9. The frequency-dependent permittivity and conductivity values of the tissue-mimicking human bone phantom.

Table 4.6. The comparison of the computed electrical values of the human average phantom and values in ANSYS HFSS value at 1 GHz.

	Real Value	**Computed Value**	**Deviation ratio**
Relative Permittivity	31	33.19	7.06%
Conductivity (S/m)	0.8	0.77	3.75%

Table 4.7. The comparison of the computed electrical values of the human bone phantom and values in ANSYS HFSS value at 1 GHz.

	Real Value	**Computed Value**	**Deviation ratio**
Relative Permittivity	16.47	16.58	0.66%
Conductivity (S/m)	0.26	0.25	3.8%

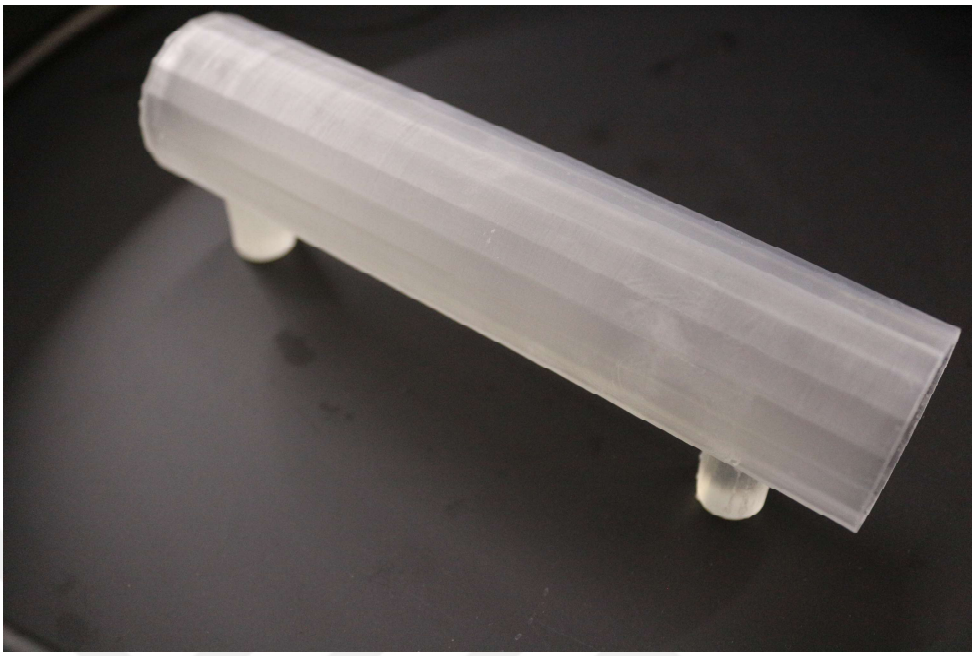

(a)

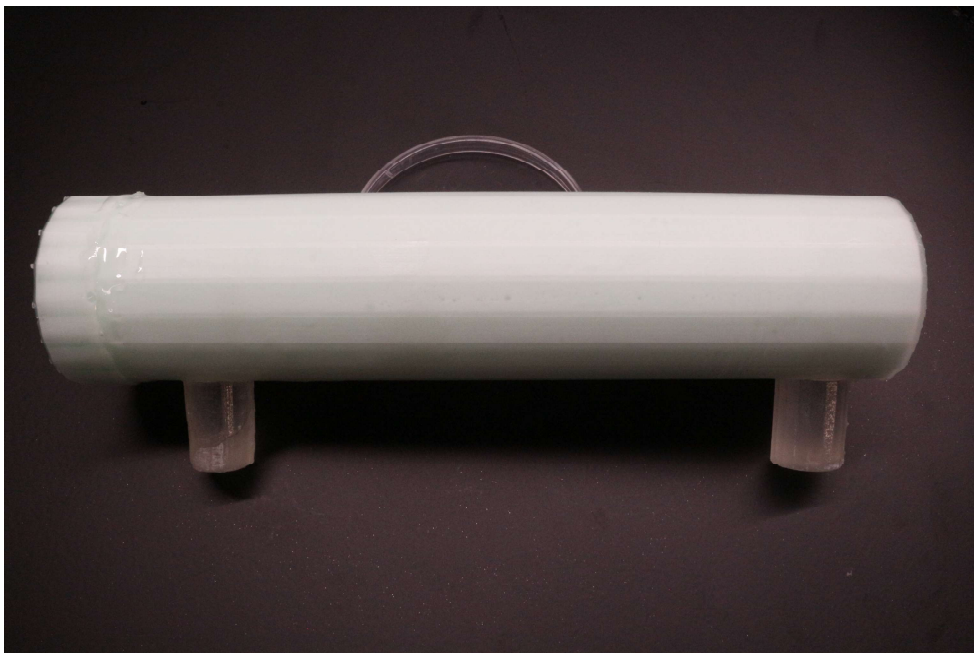

(b)

Figure 4.10. 3D printed empty (a) and filled with human bone phantom (b) cylindrical model.

The discrepancy between the real and computed values is predicted to be caused by the evaporation of water throughout the fabrication. This discrepancy can be presented as percent error. As can be seen in Table 4.6 and Table 4.7, the deviation ratio for each case is less than 10%. Thus, the discrepancy can be counted within the limits of the manufacturing accuracy.

4.2.4. Cleaning Procedure of Mg Suture

The cleaning procedure of magnesium-based suture consists of the utilization of three different chemicals such as n-hexane, acetone and ethanol. Also, a suitable beaker glass should be selected according to the quantity and size of the samples. It is important to fill up the ultrasonic bath with distilled water for 2/3.

The following cleaning process is listed as below;

- Filling the beaker with n-hexane and sample, as shown in Figure 4.11.
- Clean the sample for 20 minutes in the ultrasonic bath with n-hexane.
- Remove the n-hexane from the beaker glass.
- Filling the beaker with acetone and sample, as shown in Figure.
- Clean the sample for 20 minutes in the ultrasonic bath with acetone.
- Remove the acetone from the beaker glass.
- Filling the beaker with ethanol and sample, as shown in Figure.
- Clean the sample for 3 minutes in the ultrasonic bath with ethanol.
- Remove the acetone from the beaker glass.

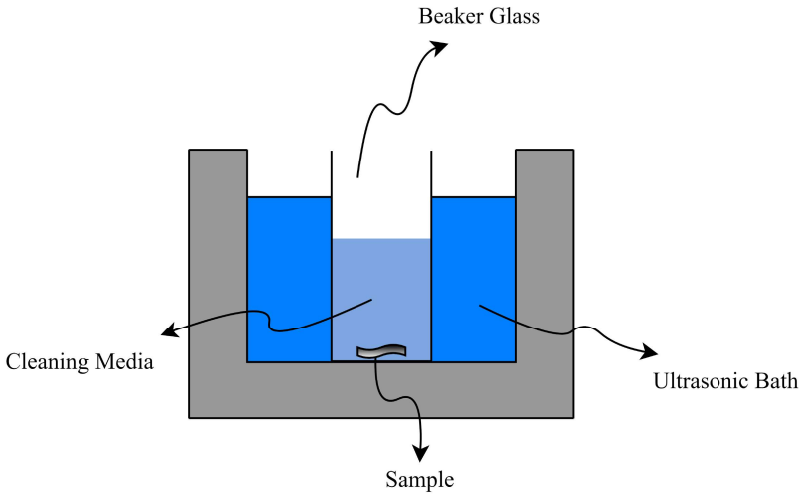

Figure 4.11. The cleaning mechanism of Mg-based suture in the ultrasonic bath.

4.3. The Completed Measurement Setup

The plexiglass container with 20 cm x 20 cm x 10 cm is designed to realize the measurements, as shwon in Figure 4.12. The human model in Figure 4.10 is placed on the plexiglass setup. The reader antenna is positioned at the bottom of the plexiglass setup. Then, the rest of the container is filled with human average phantom shown in Figure 4.12.

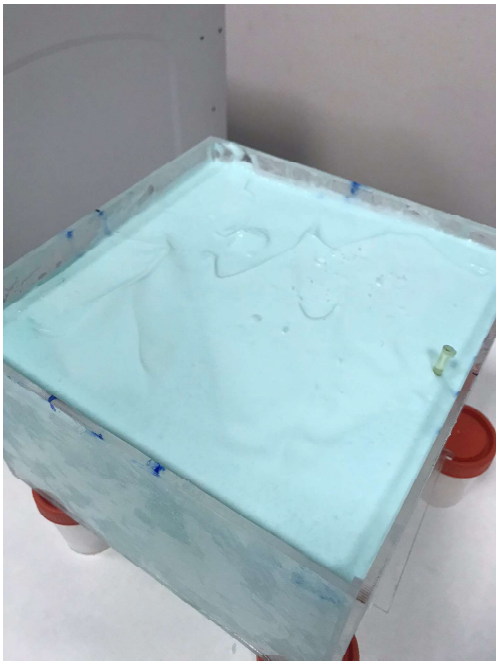

Figure 4.12. The completed measurement setup.

4.4. On-Body Results and Discussion

Figure 4.13 shows the simulated and measured frequency response of the degradation of single Mg-based suture on the different thicknesses human average phantom. In the simulation model, the degradation of the magnesium suture is tracked up to 30 mm human average phantom. However, in the measurement setup, the degradation tracking is achieved up to 25 mm human average phantom.

The different positions of Mg-based suture on the human bone model were analyzed. Figure 4.14 compares the measured and simulated frequency responses of degraded and nondegraded cases of the Mg-based suture for the different positions of the suture relative to the reader antenna. In the measurement setup, the degradation tracking fails when the alignment is changed.

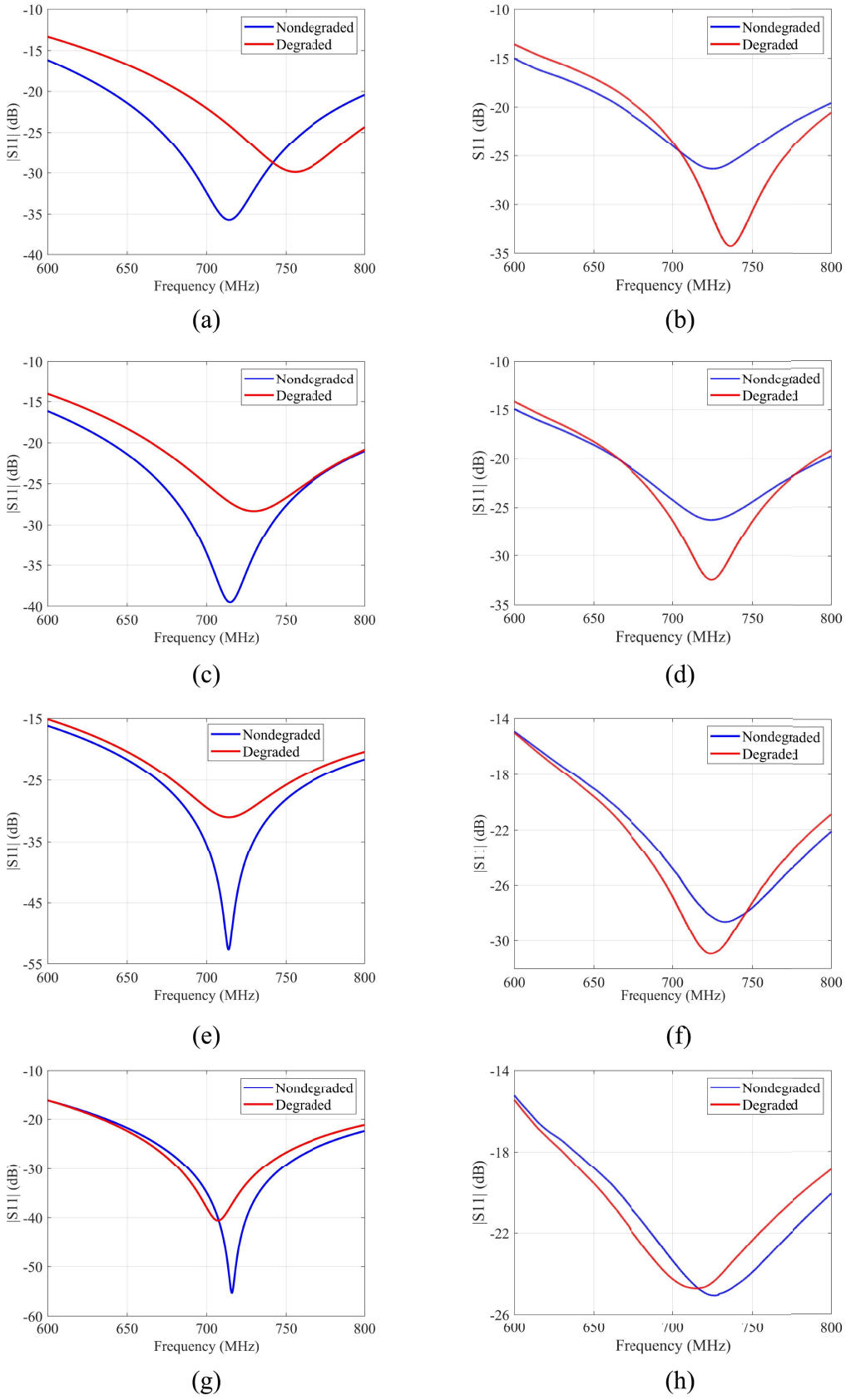

Figure 4.13. The frequency responses of the degraded and nondegraded cases of the Mg-based suture for the simulated (a),(c),(e),(g) and measured (b),(d),(f),(h) at 1.5 cm, 2 cm, 2.5 cm and 3 cm human average layer thickness,respectively.

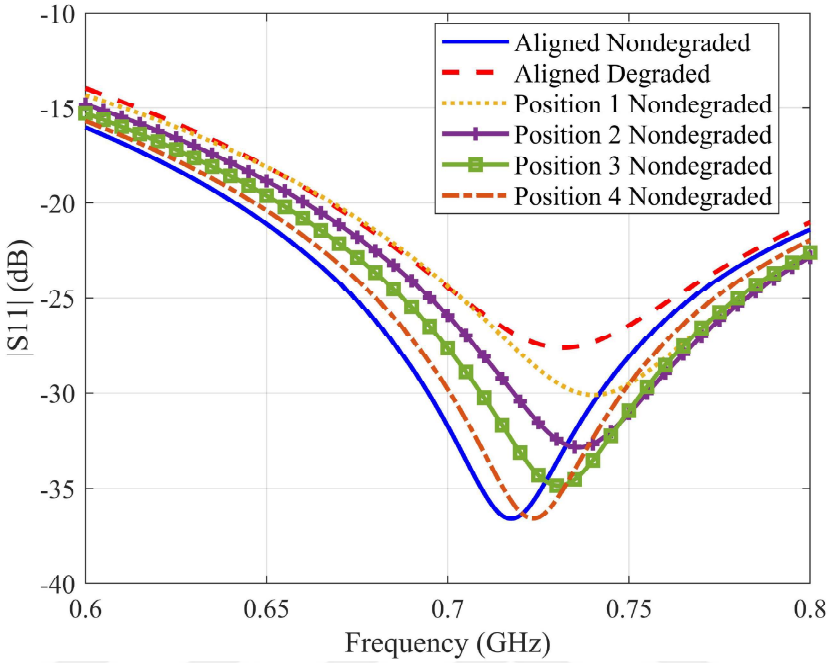

(a)

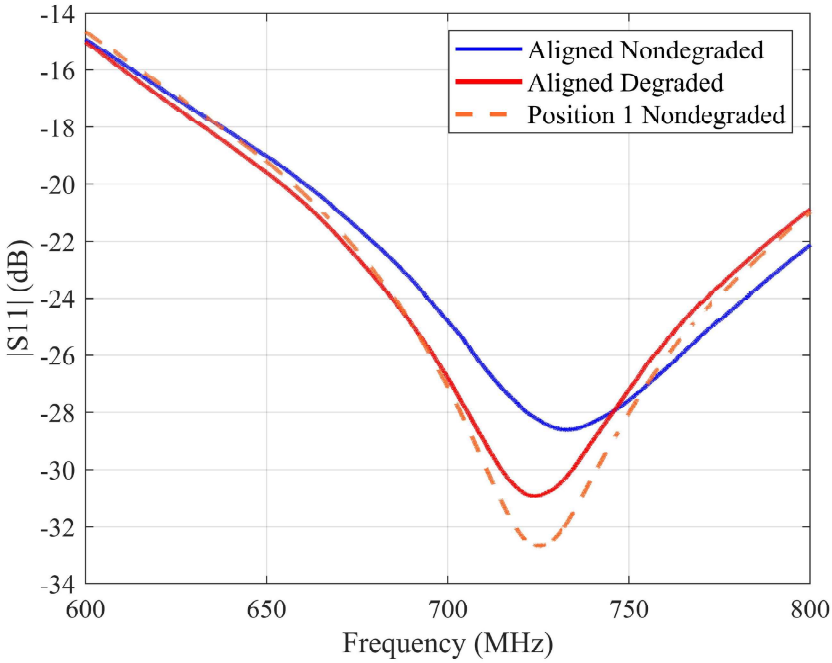

(b)

Figure 4.14. The frequency response of the degraded and nondegraded cases of the Mg-based suture for the simulated (a) and measured (b) model at different positions of the Mg-based suture on the bone.

5. CONCLUSION

Open heart surgery is one of the ways to treat several heart diseases. However, due to the surgical site's sensitivity and the operation's difficulty, monitoring the patient becomes a critical topic in the postoperative process. After the surgeries, sutures made of stainless steel or titanium are usually preferred to close the sternum. However, in recent years, the use of biodegradable metals for this suture has been discussed. Magnesium has become an attractive material due to its biocompatibility level, mechanical properties, its degradation process in which the human body does not form any byproduct.

This thesis proposes a wearable antenna system that monitors the structural state of the magnesium-based sutures surrounding the sternum in the body. Ultra-wideband(UWB) coplanar waveguide(CPW) fed circular disc monopole antenna is designed as an on-body reader antenna. The antenna is then optimized to operate on the human body. In the numeric model, the degradation of magnesium, the breakage detection on magnesium suture, different layer thickness between the antenna and magnesium suture, and the different position of suture on bone relative to the antenna are analyzed. Then, the antenna is fabricated using Rogers RO3210 with relative permittivity of 10.2. Also, the tissue-mimicking phantoms for human average and human bone are prepared to evaluate the on-body performance of the antenna. Finally, simulation and measurement results are compared and interpreted. The degradation of the magnesium suture can be tracked up to 25 mm human average layer thickness between the suture and the reader antenna. The position of the mg suture relative to the reader antenna becomes an important point since it directly effects the degradation tracking. Although the monitoring of the degradation of the magnesium suture can achieved, there are some inconsistencies between the simulation and measurement results. To address these problems, the measurement setup can be enlarged to represent the human chest area well.

REFERENCES

1. for Disease Control, C. and Prevention, "About Multiple Cause of Death, 1999-2020", 2022, https://www.cdc.gov/heartdisease/facts.htm, accessed in February 21, 2022.

2. Virani, S. S., A. Alonso, H. J. Aparicio, E. J. Benjamin, M. S. Bittencourt, C. W. Callaway, A. P. Carson, A. M. Chamberlain, S. Cheng, F. N. Delling, M. S. Elkind, K. R. Evenson, J. F. Ferguson, D. K. Gupta, S. S. Khan, B. M. Kissela, K. L. Knutson, C. D. Lee, T. T. Lewis, J. Liu, M. S. Loop, P. L. Lutsey, J. Ma, J. Mackey, S. S. Martin, D. B. Matchar, M. E. Mussolino, S. D. Navaneethan, A. M. Perak, G. A. Roth, Z. Samad, G. M. Satou, E. B. Schroeder, S. H. Shah, C. M. Shay, A. Stokes, L. B. VanWagner, N.-Y. Wang and C. W. Tsao, "Heart Disease and Stroke Statistics—2021 Update", *Circulation*, Vol. 143, No. 8, pp. 254–743, 2021.

3. Foundation, B. H., "Number of Inpatient Episodes with a Main Diagnosis of Circulatory System Disease in the United Kingdom (UK) from 2012/13 to 2020/21, by disease", accessed in April 2022, https://www.statista.com/statistics/946113/.

4. Foundation, B. H., "Deaths from Coronary Heart Disease in the United Kingdom (UK) in 2020, by country", accessed in April 2022, https://www.statista.com/statistics/940705.

5. Foundation, B. H., "Deaths from Cardiovascular Disease in the United Kingdom (UK) in 2021, by country", accessed in April 2022, https://www.statista.com/statistics/940632/.

6. Foundation, B. H., "Annual Number of Coronary Artery Bypass Surgeries in the United Kingdom (UK) from 2000 to 2019/20", accessed in April 2022, https://www.statista.com/statistics/940785.

7. Service, N. H., "Average Cost of Heart Treatments and Procedures on the NHS in the United Kingdom (UK) in 2016", February 2016, https://www.statista.com/statistics/686738.

8. Clinic, C., "Open Heart Surgery", March 2021, https://my.clevelandclinic.org/health/treatments/21502.

9. Cove, M. E., D. W. Spelman and G. MacLaren, "Infectious Complications of Cardiac Surgery: A Clinical Review", *National Institutes of Health*, Vol. 26, No. 6, pp. 1094–1100, 2012.

10. Omran, A. S., A. Karimi, S. H. Ahmadi, S. Davoodi, M. Marzban, N. Movahedi, K. Abbasi, M. A. Boroumand, S. Davoodi and N. Moshtaghi, "Superficial and Deep Sternal Wound Infection After More Than 9000 Coronary Artery Bypass Graft (CABG): Incidence, Risk Factors and Mortality", *BMC Infectious Diseases*, Vol. 7, p. 112, 2007.

11. Baillot, R., D. Cloutier, L. Montalin, L. Côté, F. Lellouche, C. Houde, G. Gaudreau and P. Voisine, "Impact of Deep Sternal Wound Infection Management with Vacuum-Assisted Closure Therapy followed by Sternal Osteosynthesis: a 15-Year Review of 23,499 Sternotomies", *Eur J Cardiothorac Surg*, Vol. 37, No. 4, pp. 880–887, 2010.

12. Kwong, R. Y. and E. K. Yucel, "Computed Tomography Scan and Magnetic Resonance Imaging", *Circulation*, Vol. 108, No. 15, pp. 104–106, 2003.

13. Morin, R. L., T. C. Gerber and C. H. McCollough, "Radiation Dose in Computed Tomography of the Heart", *Circulation*, Vol. 107, No. 6, pp. 917–922, 2003.

14. Watson, S., "Can CT Scans Lead to Cancer?", https://www.webmd.com/cancer/can-ct-scans-lead-to-cancer.

15. Vasilescu, L., M. Faller and A. Allou, "Assessment of the Unit Costs in Imag-

ing acts: the Example of MRI and CT-scan Acts in France", *ISPOR Europe*, Barcelona,Spain, 2018.

16. Ararat, K., O. Altan, S. Serbest, O. Baser and S. Dumanli, "A Biodegradable Implant Antenna Detecting Post-Surgical Infection", *14th European Conference on Antennas and Propagation (EuCAP)*, Copenhagen,Denmark, 2020.

17. Jones, E. M., C. A. Cochrane and S. L. Percival, "The Effect of pH on the Extracellular Matrix and Biofilms", *Advances in Wound Care*, Vol. 4, No. 7, pp. 431–439, 2015.

18. Manivasagam, G., D. Dhinasekaran and A. Rajamanickam, "Biomedical Implants: Corrosion and its Prevention - A Review", *Recent Patents on Corrosion Science*, Vol. 2, pp. 40–54, 2010.

19. Haffner, S., *Multiple Drug Resistance in Cancer 2: Molecular, Cellular and Clinical Aspects*, Springer, Netherlands, Dordrecht, 1998.

20. Seitz, J.-M., D. Utermöhlen, E. Wulf, C. Klose and F.-W. Bach, "The Manufacture of Resorbable Suture Material from Magnesium – Drawing and Stranding of Thin Wires", *Advanced Engineering Materials*, Vol. 13, No. 12, pp. 1087–1095, 2011.

21. Naleway, S. E., W. Lear, J. J. Kruzic and C. B. Maughan, "Mechanical Properties of Suture Materials in General and Cutaneous Surgery", *Journal of Biomedical Materials Research Part B: Applied Biomaterials.*, Vol. 103, No. 4, pp. 735–742, 2015.

22. Yao, J., T. Korotkova and R. L. Smith, "Viability and Proliferation of Pluripotential Cells Delivered to Tendon Repair Sites Using Bioactive Sutures—An In Vitro Study", *The Journal of Hand Surgery*, Vol. 36, No. 2, pp. 252–258, 2011.

23. Neligan, P. C., "Bioactive Sutures", *Plastic and Reconstructive Surgery*, Vol. 118,

No. 7, pp. 1645–1647, 2006.

24. Stamboulis, A., L. L. Hench and A. R. Boccaccini, "Mechanical Properties of Biodegradable Polymer Sutures Coated with Bioactive Glass", *Journal of Materials Science: Materials in Medicine*, Vol. 13, No. 9, pp. 843–848, 2002.

25. Middleton, J. C. and A. J. Tipton, "Synthetic Biodegradable Polymers as Orthopedic Devices", *Biomaterials*, Vol. 21, No. 23, pp. 2335–2346, 2000.

26. Flick, H., "Synthetic, Absorbable Suture in Eye-Muscle Surgery", *Albrecht von Graefes Arch. Klin. Ophthalmol*, Vol. 205, No. 1, pp. 1–8, 1977.

27. Amass, W., A. Amass and B. Tighe, "A Review of Biodegradable Polymers: Uses, Current Developments in the Synthesis and Characterization of Biodegradable Polyesters, Blends of Biodegradable Polymers and Recent Advances in Biodegradation Studies", *Polymer International*, Vol. 47, No. 2, pp. 89–144, 1988.

28. Nair, L. S. and C. T. Laurencin, "Biodegradable Polymers as Biomaterials", *Progress in Polymer Science*, Vol. 32, No. 8-9, pp. 762–798, 2007.

29. Claes, L. E., "Mechanical Characterization of Biodegradable Implants", *Clinical Materials*, Vol. 10, No. 1-2, pp. 41–46, 1992.

30. Song, G. and S. Song, "A Possible Biodegradable Magnesium Implant Material", *Advanced Engineering Materials*, Vol. 9, No. 4, pp. 298–302, 2007.

31. Witte, F., V. Kaese, H. Haferkamp, E. Switzer, A. Meyer-Lindenberg, C. J. Wirth and H. Windhageng, "In Vivo Corrosion of Four Magnesium Alloys and the Associated Bone Response", *Biomaterials*, Vol. 26, No. 17, pp. 3557–3563, 2005.

32. Staiger, M. P., A. M. Pietak, J. Huadmai and G. Dias, "Magnesium and its Alloys as Orthopedic Biomaterials: A Review", *Biomaterials*, Vol. 27, No. 9, pp. 1728–1734, 2006.

33. Song, G., "Control of Biodegradation of Biocompatable Magnesium Alloys", *Corrosion Science*, Vol. 49, No. 4, pp. 1696–1701, 2007.

34. Mueller, P. P., S. Arnold, M. Badar, D. Bormann, F.-W. Bach, A. Drynda, A. Meyer-Lindenberg, H. Hauser and M. Peuster, "Histological and Molecular Evaluation of Iron as Degradable Medical Implant Material in a Murine Animal Model", *Journal of Biomedical Materials Research Part A*, Vol. 100A, No. 11, pp. 2881–2889, 2012.

35. Bowen, P. K., J. Drelich and J. Goldman, "Zinc Exhibits Ideal Physiological Corrosion Behavior for Bioabsorbable Stents", *Advanced Materials*, Vol. 25, No. 18, pp. 2577–2582, 2013.

36. Gu, X., Y. Zheng, Y. Cheng, S. Zhong and T. Xi, "In Vitro Corrosion and Biocompatibility of Binary Magnesium Alloys", *Biomaterials*, Vol. 30, No. 4, pp. 484–498, 2009.

37. Waizy, H., J. M. Seitz, J. Reifenrath, A. Weizbauer, F. W. Bach, A. Meyer-Lindenberg, B. Denkena and H. Windhagen, "Biodegradable Magnesium Implants for Orthopedic Applications", *Journal of Materials Science*, Vol. 30, No. 4, pp. 38–50, 2013.

38. Hamid, H. and J. Coltart, "Miracle Stents' - A Future without Restenosis", *McGill Journal of Medicine*, Vol. 10, No. 2, pp. 105–111, 2007.

39. Niestroj, I., *Praxis der Orthomolekularen Medizin: Physiologische Grundlagen, Therapie mit Mikro-Nährstoffen*, Hippokratess, Stuttgart, 2001.

40. Schmidt, R. F., G. Thews and F. Lang, *Physiologie des Menschen*, Springer, Berlin, 2005.

41. Feyerabend, F., J. Fischer, J. Holtz, F. Witte, R. Willumeit, H. Drücker, C. Vogt and N. Hort, "'Evaluation of Short-Term Effects of Rare Earth and Other Ele-

ments used In Magnesium Alloys on Primary Cells and Cell Lines", *Acta Biomaterialia*, Vol. 6, No. 5, pp. 1834–1842, 2010.

42. Willbold, E., X. Gu, D. Albert, K. Kalla, K. Bobe, M. Brauneis, C. Janning, J. Nellesen, W. Czayka, W. Tillmann, Y. Zheng and F. Witte, "Effect of the Addition of Low Rare Earth Elements (lanthanum, neodymium, cerium) on the Biodegradation and Biocompatibility of Magnesium", *Acta Biomaterialia*, Vol. 11, pp. 554–562, 2015.

43. Drynda, A., N. Deinet, N. Braun and M. Peuster, "Rare Earth Metals used in Biodegradable Magnesium-Based Stents Do Not Interfere with Proliferation of Smooth Muscle Cells but Do Induce the Upregulation of Inflammatory Genesm", *Journal of Biomedical Materials Research Part A*, Vol. 91A, No. 2, pp. 360–369, 2009.

44. Fosmire, G. J., "Zinc Toxicity", *The American Journal of Clinical Nutrition*, Vol. 51, No. 2, pp. 225–227, 1990.

45. Schümann, K., T. Ettle, B. Szegner, B. Elsenhans and N. W. Solomons, "On Risks and Benefits of Iron Supplementation Recommendations for Iron Intake Revisited", *Journal of Trace Elements in Medicine and Biology*, Vol. 21, No. 3, pp. 147–168, 2007.

46. Nriagu, J., *Encyclopedia of Environmental Health*, Elsevier, Oxford, 2007.

47. Seitz, J. M., R. Eifler, F. W. Bach and H. J. Maier, "Magnesium Degradation Products: Effects on Tissue and Human Metabolism", *Journal of Biomedical Materials Research Part A*, Vol. 102, No. 10, pp. 3744–3753, 2014.

48. Seitz, J.-M., M. Durisin, J. Goldman and J. W. Drelich, "Recent Advances in Biodegradable Metals for Medical Sutures: A Critical Review", *Advanced Healthcare Materials*, Vol. 4, No. 13, pp. 1915–1936, 2015.

49. Seitz, J.-M., E. Wulf, P. Freytag, D. Bormann and F.-W. Bach, "The Manufacture of Resorbable Suture Material from Magnesium", *Advanced Engineering Materials*, Vol. 12, No. 11, pp. 1099–1105, 2010.

50. Kirkland, N. T., J. Lespagnol, N. Birbilis and M. P. Staiger, "A Survey of Bio-Corrosion Rates of Magnesium Alloys", *Corrosion Sciences*, Vol. 52, No. 2, pp. 287–2915, 2010.

51. Witte, F., J. Fischer, J. Nellesen, H.-A. Crostack, V. Kaese, A. Pisch, F. Beckmann and H. Windhagen, "In Vitro and in Vivo Corrosion Measurements of Magnesium Alloys", *Biomaterials*, Vol. 27, No. 7, pp. 1013–1018, 2006.

52. Atrens, A., G.-L. Song, F. Cao, Z. Shi and P. K. Bowen, "Advances in Mg Corrosion and Research Suggestions", *Journal of Magnesium and Alloys*, Vol. 1, No. 3, pp. 177–200, 2013.

53. Zheng, Y. F., X. N. Gu, and F. Witte, "Biodegradable Metals", *Materials Science and Engineering: R: Reports*, Vol. 77, pp. 1–34, 2014.

54. Sezgen, O. F., O. K. Erden, N. Haciosmanoglu, M. E. Lacin, A. D. Yalcinkaya, Z. C. C. Ozdil, U. O. S. Seker and S. Dumanli, "A Repeater Antenna System Utilizing Genetically Modified Bacteria for Multiscale Communications", *16th European Conference on Antennas and Propagation (EuCAP)*, Madrid,Spain, 2022.

55. Vert, M., J. Mauduit and S. Li, "Biodegradation of PLA/GA Polymers: Increasing Complexity", *Biomaterials*, Vol. 15, No. 15, pp. 1209–1213, 1994.

56. Moravej, M., A. Purnama, M. Fiset, J. Couet and D. Mantovanii, "Electroformed Pure Iron as A New Biomaterial for Degradable Stents: In Vitro Degradation and Preliminary Cell Viability Studies", *Acta Biomaterialias*, Vol. 6, No. 5, pp. 1843–1851, 2010.

57. Song, G. and A. Atrens, "Understanding Magnesium Corrosion—A Framework

for Improved Alloy Performance", *Advanced Engineering Materials*, Vol. 5, No. 12, pp. 837–858, 2003.

58. Baril, G., G. Galicia, C. Deslouis, N. Pébère, B. Tribollet and V. Vivier, "An Impedance Investigation of the Mechanism of Pure Magnesium Corrosion in Sodium Sulfate Solutions", *Journal of The Electrochemical Society*, Vol. 154, No. 2, p. C108, 2006.

59. Zhang, X. G., *Corrosion and Electrochemistry of Zinc*, Plenum Press, New York, 1996.

60. Fu, K., D. W. Pack, A. M. Klibanov and R. Langer, "Visual Evidence of Acidic Environment Within Degrading Poly(lactic-co-glycolic acid) (PLGA) Microspheres", *Pharmaceutical Research*, Vol. 17, No. 1, pp. 100–106, 2000.

61. Sung, H.-J., C. Meredith, C. Johnson and Z. S. Galis, "The Effect of Scaffold Degradation Rate on Three-Dimensional Cell Growth and Angiogenesis", *Biomaterials*, Vol. 25, No. 26, pp. 5735–5742, 2004.

62. Li, Z., X. Gu, S. Lou and Y. Zheng, "The Development of Binary Mg–Ca Alloys for Use as Biodegradable Materials within Bone", *Biomaterials*, Vol. 29, No. 10, pp. 1329–1344, 2008.

63. Wang, F. and G. Wang, "Design of a 20-element Inkjet-Printed Antenna Array for Wearable Microwave Breast Imaging and Diagnosis", *2017 International Conference on Electromagnetics in Advanced Applications (ICEAA)*, Verona, Italy, 2017.

64. Elsheikh, D. and A. R. Eldamak, "Microwave Textile Sensors for Breast Cancer Detection", *38th National Radio Science Conference (NRSC)*, Mansoura,Egypt, 2021.

65. Alsharif, F. and C. Kurnaz, "Wearable Microstrip Patch Ultra Wide Band An-

tenna for Breast Cancer Detection", *41st International Conference on Telecommunications and Signal Processing (TSP)*, Athens,Greece, 2018.

66. Wang, F. and T. Arslan, "A Thin-Film-Based Wearable Antenna Array for Breast Microwave Imaging and Diagnosis", *First IEEE MTT-S International Microwave Bio Conference (IMBIOC)*, Gothenburg,Sweden, 2017.

67. Porter, E., H. Bahrami, A. Santorelli, B. Gosselin, L. A. Rusch and M. Popović, "Wearable Microwave Antenna Array for Time-Domain Breast Tumor Screening", *IEEE Transactions on Medical Imaging*, Vol. 35, No. 6, pp. 1501–1509, June 2016.

68. Ozcakar, E., O. Sayginer and G. Kiziltas, "Design of a Wearable Microwave Antenna System for Breast Tumor Imaging", *2021 International Applied Computational Electromagnetics Society Symposium (ACES)*, Hamilton,Canada, 2021.

69. Bhavani, S., "Wearable Microstrip Circular Patch Antenna for Breast Cancer Detection", *2021 IEEE International Symposium on Antennas and Propagation and USNC-URSI Radio Science Meeting (APS/URSI)*, Singapore, 2021.

70. Paul, M. R., M. L. Moses, T. Perarasi and R. Kannan, "Ultra-Wideband Flexible and Wearable Textile Antenna for Predicting Breast Cancer", *2021 Smart Technologies, Communication and Robotics (STCR)*, Sathyamangalam,India, 2021.

71. Wang, F., T. Arslan and G. Wang, "Breast Cancer Detection with Microwave Imaging System Using Wearable Conformal Antenna Arrays", *IEEE International Conference on Imaging Systems and Techniques (IST)*, Beijing,China, 2017.

72. Bahramiabarghouei, H., E. Porter, A. Santorelli, B. Gosselin, M. Popović and L. A. Rusch, "Flexible 16 Antenna Array for Microwave Breast Cancer Detection", *IEEE Transactions on Biomedical Engineering*, Vol. 62, No. 10, pp. 2516–2525, October 2015.

73. Wang, C., R. Goel, M. Noun, R. K. Ghanta and B. Najafi, "Wearable Sensor-

Based Digital Biomarker to Estimate Chest Expansion During Sit-to-Stand Transitions–A Practical Tool to Improve Sternal Precautions in Patients Undergoing Median Sternotomy", *IEEE Transactions on Neural Systems and Rehabilitation Engineering*, Vol. 28, No. 1, pp. 165–173, 2020.

74. Kachel, E., K. Constantini, D. Nachman, S. Carasso, R. Littman, A. Eisenkraft and Y. Gepner, "A Pilot Study of Blood Pressure Monitoring After Cardiac Surgery Using a Wearable, Non-invasive Sensor", *Frontiers in Medicine*, Vol. 8, 2021.

75. Särestöniemi, M., C. Pomalaza-ráez, Z. Bi, T. Kumpuniemi, C. Kissi, M. Sonkki, M. Hämäläinen and J. Iinattit, "Comprehensive Study on the Impact of Sternotomy Wires on UWB WBAN Channel Characteristics on the Human Chest Area", *IEEE Access*, Vol. 7, pp. 74670 – 74682, 2019.

76. Yang, W.-B., K. Sayrafian-Pour, J. Hagedorn, J. Terrill, K. Y. Yazdandoost, A. Taparugssanagorn, M. Hämäläinen and J. Iinatti, "Impact of An Aortic Valve Implant on Body Surface UWB Propagation: A Preliminary Study", *5th Int. Symp. Med. Inf. Commun. Technol.*, Montreux,Switzerland, 2011.

77. Särestöniemi, M., T. Kumpuniemi, M. Hämäläinen, J. Iinatti and C. Pomalaza-Raéz, "Impact of the Sternotomy Wires and Aortic Valve Implant on the On-Body UWB Radio Channel", *12th International Symposium on Medical Information and Communication Technology (ISMICT)*, Sydney,Australia, 2018.

78. Särestöniemi, M., C. Pomalaza-Ráez, T. Kumpuniemi, M. Hämäläinen, R. Kovacs and J. Iinatti, "Measurement Data Based Study on the Intra-Body Propagation in the Presence of the Sternotomy Wires and Aortic Valve Implant", *IEEE Trans. Antennas Propag.*, Vol. 67, No. 8, pp. 4989 – 5001, 2019.

79. Särestöniemi, M., C. Pomalaza-Ráez, T. Kumpuniemi, M. Hämäläinen and J. Iinatti, "A Finite Integration Technique Based Simulation Study on the Impact of the Sternotomy Wires on the UWB Channel Characteristics", *Proc. Int. Symp.*

Wireless Body Area Netw. (BodyNets), Oulu,Finland, 2018.

80. Balanis, C. A., *Antenna Theory: Analysis and Design*, Wiley–Blackwell, 2016.

81. Das, N. K., *The Electrical Engineering Handbook*, Academic Press, 2005.

82. Liang, J., L. Guo, C. Chiau and X. Chen, "CPW-Fed Circular Disc Monopole Antenna for UWB Applications", *IWAT 2005. IEEE International Workshop on Antenna Technology: Small Antennas and Novel Metamaterials,*, Singapore, 2005.

83. Srifi, M. N., S. K. Podilchak, M. Essaaidi and Y. M. Antar, "Planar Circular Disc Monopole Antennas Using Compact Impedance Matching Networks for Ultra-wideband (UWB) Applications", *Asia Pacific Microwave Conference*, Singapore, 2010.

84. Liang, J., C. Chiau, X. Chen and C. Parini, "Study of A Printed Circular Disc Monopole Antenna for UWB Systems", *IEEE Transactions on Antennas and Propagation*, Vol. 53, No. 11, pp. 3500–3504, 2005.

85. Srifi, M. N., S. K. Podilchak, M. Essaaidi and Y. M. M. Antar, "Compact Disc Monopole Antennas for Current and Future Ultrawideband (UWB) Applications", *IEEE Transactions on Antennas and Propagation*, Vol. 59, No. 12, pp. 4470 – 4480, 2011.

86. Kundu, S. and S. K. Jana, "A Compact Planar CPW Fed Monopole Antenna for Ultra Wideband Applications", *14th IEEE India Council International Conference (INDICON)*, Roorkee,India, 2018.

87. Zhang, Y., T. Nakata and T. Miyashita, "A Miniature Circular Disc Monopole UWB Antenna with a Tapered Feed Line and a Circular Ground", *China-Japan Joint Microwave Conference*, Shanghai,China, 2008.

88. Chen, N.-W. and Y.-C. Liang, "Coplanar-Waveguide Fed Circular Disc Monopole Antenna with Improved Radiation Characteristics", *The Second European Con-*

ference on Antennas and Propagation, EuCAP, Edinburgh,Scotland, 2008.

89. Chahine, S. A., M. Addam, H. A. Rahim, A. Itani and H. Jomaa, "A Modified Circular Disc Monopole Ultra Wide Band antenna", *International Conference on Advances in Computational Tools for Engineering Applications*, Beirut,Lebanon, 2009.

90. Kumar, R. and P. Bansode, "On the Design of Ultra Wide Band Antenna Based on Fractal Geometry", *ITU-T Kaleidoscope: Beyond the Internet? - Innovations for Future Networks and Services*, Pune,India, 2010.

91. Ghanbari, L., S. Nikmehr and M. Rezvani, "A Novel Small UWB Antenna Using New Fractal-like Geometry", *IEEE Applied Electromagnetics Conference (AEMC)*, Kolkata,India, 2011.

92. Kumar, R., R. R. Krishna and N. Kushwaha, "A Fractal Monopole Antenna for UWB Applications", *IEEE Applied Electromagnetics Conference (AEMC)*, Bhubaneswar,India, 2013.

93. Chen, W.-S., S.-C. Wu and K.-N. Yang, "A Study of the Printed Heart Monopole Antenna for IEEE 802.16a/UWB applications", *IEEE Antennas and Propagation Society International Symposium*.

94. Phakaew, T., S. Chalermwisutkul, W. Thaiwirot and K. Kaemarungsi, "A Wideband Bidirectional Monkey Face Antenna for Liquid Level Sensing", *International ECTI Northern Section Conference on Electrical, Electronics, Computer and Telecommunications Engineering (ECTI-NCON)*, Chiang Rai, Thailand, 2018.

95. Faezi, H., K. Mohammadpour-Aghdam, A. R. Gholipour and R. Faraji-Dana, "A Printed Rugby Ball Monopole Antenna for UWB Applications", *The Second European Conference on Antennas and Propagation, EuCAP*, Edinburgh,Scotland, 2008.

96. Ghanem, F., "A New Switched Polarisation Antenna", *6th European Conference on Antennas and Propagation (EUCAP)*, Prague,Czech Republic, 2012.

97. Ghanem, F., J. R. Kelly and P. S. Hall, "Switched UWB to Narrowband Planar Monopole Antenna", *Proceedings of the Fourth European Conference on Antennas and Propagation*, Barcelona,Spain, 2010.

98. Tebache, S., F. Ghanem and A. Belouchrani, "Novel and Simple Approach for Reconfiguring the Pattern of An UWB CPW-Fed Monopole Antenna", *Seminar on Detection Systems Architectures and Technologies (DAT)*, Algiers, Algeria, 2017.

99. Aboufoul, T. and A. Alomainy, "Reconfigurable Printed UWB Circular Disc Monopole Antenna", *Loughborough Antennas Propagation Conference*, Loughborough, UK, 2011.

100. Kumar, A., I. B. Sharma and M. M. Sharma, "Reconfigurable Circular Disc Monopole UWB Antenna with Switchable Two Notched Stop Bands", *IEEE Annual India Conference (INDICON)*, Bangalore, Indiae, 2017.

101. Ranga, Y., A. K. Verma, K. P. Esselle and A. R. Weily, "A Gain-enhanced Semicircular Disc Antenna with a Quasi-planar Surface-mounted Short TEM Horn", *The 3rd European Wireless Technology Conference*, Paris,France, 2010.

102. Pillalamarri, R. and G. S. B. Rao, "Analysis on Size Miniaturization in Printed Circular Disc Monopole Antennas for UWB Communications", *International Conference on Ultra Modern Telecommunications Workshops*, St. Petersburg, Russia, 2009.

103. Sharma, S. and M. K. Savita, "Multi Band Circular Antenna for Ultrawideband Wireless Systems", *Nirma University International Conference on Engineering (NUiCONE)*, Ahmedabad, India, 2013.

104. Sharma, M. M., I. B. Sharma, Jaiverdhan and R. Agarwal, "Circular Edge Cut Diminutive UWB Antenna for Wireless Communications", *IEEE Indian Conference on Antennas and Propogation (InCAP)*, Ahmedabad, India, 2020.

105. Khan, M. K., M. I. Khan, I. Ahmad and M. Saleem, "Design of A Printed Monopole Antenna with Ridged Ground for Ultra Wideband Applications", *Progress in Electromagnetic Research Symposium (PIERS)*, Shanghai, China, 2016.

106. Zhao, F., H. Tang, C. Zhao, X. Gao, P. Zhuo and F. Zhang, "Design of Novel Dual Band-notched Disk Monopole Antennas", *The International Workshop on Microwave and Millimeter Wave Circuits and System Technology*, Chengdu, China, 2012.

107. Cui, Y., W. Wang, H. Zhang, W. Zhang and P. Fei, "A Printed Circular Disc Monopole Antenna with Dual Band-notched Characteristic for UWB Applications", *Proceedings of the 9th International Symposium on Antennas, Propagation and EM Theory*, Guangzhou,China, 2011.

108. Lee, C.-M., T.-C. Yo, C.-H. Luo, W.-S. Chen, C.-H. Tu and Y.-Z. Juang, "Ultra-Wideband Printed Disk Monopole Antenna with Dual-Band Notched Functions", *IEEE Annual Wireless and Microwave Technology Conference*, Clearwater Beach, FL, USA, 2007.

109. Kumar, A., I. B. Sharma, R. K. Saraswat and M. M. Sharma, "Dual Band-Notched Circular Disc Monopole UWB Antenna with Switchable Five Notched Stop Bands", *Asia-Pacific Microwave Conference (APMC)*, New Delhi, India, 2017.

110. Antoniades, M. A. and G. V. Eleftheriades, "A Compact Multiband Monopole Antenna With a Defected Ground Plane", *IEEE Antennas and Wireless Propagation Letters*, Vol. 7, pp. 652 – 655, 2008.

111. Dionigi, M. and M. Mongiardo, "Design of Via Hole Fed Printed Circular Disc Monopole Antenna for UWB Systems", *EEE-APS Topical Conference on Antennas and Propagation in Wireless Communications*, Turin, Italy, 2011.

112. Yang, X.-X., Y.-M. Lu, Y.-J. Xue and G.-X. Zheng, "Analysis on the Monopole UWB Antenna of Double-Printed Circular Disc", *IEEE Antennas and Propagation Society International Symposium*, Albuquerque, NM, USA, 2006.

113. Lingling, Z., Q. Jinghui, Z. Ning and X. Xiaohang, "Novel Ultrawide-band Miniature Antennas", *International Conference on Microwave and Millimeter Wave Technology*, Guilin, China, 2007.

114. Dey, S., N. Saha and S. Biswas, "Design and Performance Analysis of UWB Circular Disc Monopole Textile Antenna and Bending Consequences", *Proceedings of the 5th European Conference on Antennas and Propagation (EUCAP)*, Rome,Italy, 2011.

115. ANSYS, "ANSYS High Frequency Structure Simulator (HFSS)", accessed at August 2020, `http://www.ansys.com/products/electronics/ansys-hfss`.

116. Skrivervik, A. K., "Implantable antennas: The Challenge of Efficiency", *2013 7th European Conference on Antennas and Propagation (EuCAP)*, Gothenburg,Sweden, 2013.

117. Dumanli, S., "Challenges of wearable antenna design", *46th European Microwave Conference (EuMC)*, London,UK, 2005.

118. "Coplanar Waveguide Calculator", `https://microwaves101.com/calculators/`.

119. Simons, R. N., *Coplanar Waveguide Circuits, Components, and Systems*, John Wiley Sons, 2001.

120. Mobashsher, A. T. and A. M. Abbosh, "Articial Human Phantoms: Human Proxy in Testing Microwave Apparatuses That Have Electromagnetic Interaction with

the Human Body", *IEEE Microwave Magazine*, Vol. 16, No. 6, pp. 42–62, 2015.

121. García-Pardo, C., C. Andreu, A. Fornés-Leal, S. Castelló-Palacios, S. Pérez-Simbor, M. Barbi, A. Vallés-Lluch and N. Cardona, "Ultrawideband Technology for Medical In-Body Sensor Networks: An Overview of the Human Body as a Propagation Medium, Phantoms, and Approaches for Propagation Analysis", *IEEE Antennas and Propagation Magazine*, Vol. 60, pp. 19–33, 2018.

122. Pellegrini, A., A. Brizzi, L. Zhang, K. Ali, Y. Hao, X. Wu, C. C. Constantinou, Y. Nechayev, P. S. Hall, N. Chahat, M. Zhadobov and R. Sauleau, "Antennas and Propagation for Body-Centric Wireless Communications at Millimeter-Wave Frequencies: A Review [Wireless Corner]", *IEEE Antennas and Propagation Magazine*, Vol. 55, No. 4, pp. 262–287, 2013.

123. Guraliuc, A. R., M. Zhadobov, O. D. Sagazan and R. Sauleau, "Solid Phantom for Body-Centric Propagation Measurements at 60 GHz", *IEEE Transactions on Microwave Theory and Techniques*, Vol. 62, No. 6, pp. 1373–1380, 2014.

124. Mobashsher, A. T. and A. M. Abbosh, "Three-Dimensional Human Head Phantom with Realistic Electrical Properties and Anatomy", *IEEE Antennas and Wireless Propagation Letters*, Vol. 13, pp. 1401–1404, 2014.

125. Cil, E. and S. Dumanli, "Characterization of an Implanted Antenna inside a 3D Printed Multilayer Hip Phantom", *7th European Conference on Antennas and Propagation (EuCAP)*, Krakow,Poland, 2019.

126. Ruvio, G., R. Solimene, A. Cuccaro, J. E. Browne, D. Gaetano and M. J. Ammann, "Experimental Microwave Breast Cancer Detection with Oil-on-Gelatin Phantom", *International Conference on Electromagnetics in Advanced Applications (ICEAA)*, Turin,Italy, 2013.

127. Joachimowicz, N., C. Conessa, T. Henriksson and B. Duchêne, "Breast Phantoms for Microwave Imaging", *IEEE Antennas and Wireless Propagation Letters*,

Vol. 13, pp. 1333–1336, 2014.

128. Burfeindt, M. J., T. J. Colgan, R. O. Mays, J. D. Shea, N. Behdad, B. D. V. Veen and S. C. Hagness, "MRI-Derived 3-D-Printed Breast Phantom for Microwave Breast Imaging Validation", *IEEE Antennas and Wireless Propagation Letters*, Vol. 11, pp. 1610–1613, 2012.

129. Klemm, M., J. A. Leendertz, D. Gibbins, I. J. Craddock, A. Preece and R. Benjamin, "Microwave Radar-Based Breast Cancer Detection: Imaging in Inhomogeneous Breast Phantoms", *IEEE Antennas and Wireless Propagation Letters*, Vol. 8, p. 1349–1352, 2009.

130. Çil, E., *A Reconfigurable Wearable Slot Antenna Design Suitable for Smart Glasses*, Master's Thesis, Boğaziçi University, 2018.